APPENDIX N

WASTE PACKAGE AND DRIP SHIELD MATERIALS: PASSIVE FILM CHARACTERISTICS, GROWTH, AND STABILITY (RESPONSE TO CLST 1.08 AND CLST 1.09)

Note Regarding the Status of Supporting Technical Information

This document was prepared using the most current information available at the time of its development. This Technical Basis Document and its appendices providing Key Technical Issue Agreement responses that were prepared using preliminary or draft information reflect the status of the Yucca Mountain Project's scientific and design bases at the time of submittal. In some cases this involved the use of draft Analysis and Model Reports (AMRs) and other draft references whose contents may change with time. Information that evolves through subsequent revisions of the AMRs and other references will be reflected in the License Application (LA) as the approved analyses of record at the time of LA submittal. Consequently, the Project will not routinely update either this Technical Basis Document or its Key Technical Issue Agreement appendices to reflect changes in the supporting references prior to submittal of the LA.

APPENDIX N

WASTE PACKAGE AND DRIP SHIELD MATERIALS: PASSIVE FILM CHARACTERISTICS, GROWTH, AND STABILITY (RESPONSE TO CLST 1.08 AND CLST 1.09)

This appendix provides a response to Key Technical Issue (KTI) agreements Container Life and Source Term (CLST) 1.08 and 1.09. These KTI agreements relate to the formation, growth, and long-term stability of protective passive films on the surface of Alloy 22 (UNS N06022) and titanium materials under repository conditions.

N.1 KEY TECHNICAL ISSUE AGREEMENTS

N.1.1 CLST 1.08 and CLST 1.09

Agreements CLST 1.08 and CLST 1.09 were reached during the U.S. Nuclear Regulatory Commission (NRC)/U.S. Department of Energy (DOE) Technical Exchange and Management Meeting on Container Life and Source Term held September 12 and 13, 2000 (Schlueter 2000). Subissues 1, 2, 3, 4, and 6 were discussed at that meeting.

Wording of the agreements is as follows:

CLST 1.08[1]

> Provide the documentation for Alloy 22 and titanium for the path forward items listed on slide 16 and 17. DOE will provide the documentation in the revision to AMRs (ANL-EBS-MD-000003 and ANL-EBS-MD-000004) prior to LA.

CLST 1.09

> Provide the data that characterizes the passive film stability, including the welded and thermally aged specimens. DOE will provide the documentation in a revision to AMRs (ANL-EBS-MD-000003 and ANL-EBS-MD-000004) prior to LA.

N.1.2 Related Key Technical Issue Agreements

There are no other KTI agreements directly related to agreements CLST 1.08 and 1.09.

[1] The path forward items referred to on slides 16 and 17 were to (1) calculate potential-pH diagrams for multicomponent Alloy 22; (2) grow oxide films at higher temperatures in autoclaves, in air and/or electrochemically to accelerate film growth for compositional and structural studies; (3) resolve kinetics of film growth, including parabolic or higher order, whether film growth becomes linear, and if, as film grows, it becomes mechanically brittle and spalls off; (4) determine chemical, structural, and mechanical properties of films, including thickened films; (5) correlate changes in E_{corr} measured in the Long Term Corrosion Test Facility (LTCTF) with compositional changes in passive film over time; (6) perform analyses on cold-worked materials to determine changes in film structural properties; (7) perform examination of films formed on naturally occurring josephinite; and (8) compare films formed on Alloy 22 with other similar passive film alloys with longer industrial experience.

N.2 RELEVANCE TO REPOSITORY PERFORMANCE

A significant part of the corrosion resistance of the waste package and drip shield materials is due to the formation of a protective film on the surface of the materials. Data exist to show that oxide layers are formed for the expected repository environment conditions, but long-term testing in Yucca Mountain–relevant waters is still being conducted in conjunction with long-term thermal aging studies to determine the behavior of passive films on Alloy 22 at long timescales. However, short-term electrochemical testing can elucidate the conditions for the formation and breakdown of passive films on the waste package materials. These data support the evaluation of the performance of the waste package, which is a key engineered barrier system component in determining the performance of the repository.

N.3 RESPONSE

This report addresses CLST 1.08 and CLST 1.09, which discuss the nature and the stability of the oxide film. As these topics are related, they are discussed together as one document. The questions in the KTI were asked because the oxide film is responsible for kinetically limiting the dissolution of the metal by acting as a barrier layer. Thus, the oxide plays an essential role in the lifetime of the metal.

For an oxide film to be protective in a given environment, it must be chemically stable, and it must block or slow electronic and ionic transport across the film. If the film is not chemically stable, it will break down, exposing fresh metal to electrochemical dissolution, or oxidation. There is a broad base of knowledge discussing passive films and their behavior on industrial metals. To take advantage of this body of knowledge regarding performance and failure mechanisms, it is necessary to first characterize what oxides form on Alloy 22. This is a necessary first step to understanding where analogies can be drawn with other metals.

The specific issues called out in CLST 1.08 and CLST 1.09 and the sections where these issues are discussed are:

- **CLST 1.08, item 1: Calculate potential–pH diagrams (Section N.4.1)**–The solid oxide phases were calculated as a function of potential and pH for four points that correspond to experimental conditions. These data are shown in Section N.4.1 (Table N-1).

- **CLST 1.08, item 2: Grow oxide films under accelerating conditions for compositional analysis (Sections N.4.3 to N.4.5)**–Oxide growth was accelerated by applying a potential to the sample. The oxide composition was determined using x-ray photoelectron spectroscopy (XPS), Auger electron spectroscopy (AES), and electron energy-loss spectroscopy (EELS).

- **CLST 1.08, item 3: Kinetics of film growth (Section N.4.6)**–The film growth kinetics were measured for oxide film formation in pH 2.8 and 7.5 solutions. Potentiostatic current decreases exponentially with time, indicating a logarithmic increase in film stability and thickness.

- **CLST 1.08, item 4: Determine composition and mechanical property of oxides (Section N.4.5)**–The oxide composition was determined using XPS, AES, and EELS. The mechanical properties were not explicitly measured because the oxide layer responsible for passivity has never been observed to delaminate, indicating that it is well adhered to the metal substrate. At the time that the KTI agreement was written, less was known about the oxide film, and it was thought that it might thicken over time, become strained, and delaminate from the metal surface (like rust). However, as the oxide layer responsible for passivity is 4 nm or less thick, it is more deformable without being brittle and, thus, not susceptible to spalling.

- **CLST 1.08, item 5: Correlate E_{corr} with compositional changes in the passive film**–Long-term E_{corr} measurements have been made in a variety of temperature and solution environments. These data have been presented in the response to CLST 1.10 and CLST 1.11. These samples have been examined to characterize the passive film. Evaluation of the data is in progress. Preliminary findings show that the characteristics of the passive film are similar to those observed in short-term test samples in that the predominant constituent of the film is Cr_2O_3.

- **CLST 1.08, item 6: Perform analysis on cold-worked metals (Sections N.4.3 and N.4.7)**–Analysis on cold-worked samples was not explicitly performed because samples were not available. However, the analysis performed on weld samples can be applied to cold-worked metals. According to Angeliu (2001), stainless steel weldments contain up to 20% cold-work due to weld shrinkage and differential thermal expansion stresses. The composition and electrochemical behavior of weld samples did not differ significantly from base metal samples. Thus, cold-worked samples that have stresses similar to those found in welds will not have compositional or electrochemical variations from the base metal. The compositions are explicitly shown for pH values near 3 (see Section N.4.3 (Table N-3)), but this was also found to be true for samples in pH 7.5 solutions.

- **CLST 1.08, item 7: Examine oxide films on josephinite**–At the time of the agreement, josephinite was proposed as an analog material. However, josephinite is a nickel-iron alloy and has no chromium. Since the passive film that forms on Alloy 22 under a broad range of conditions is predominantly chromium oxide, the oxide film that forms on josephinite is not relevant. This conclusion was also reached by the Center for Nuclear Waste Regulatory Analyses (Cragnolino et al. 2004). No other applicable natural analogs for Alloy 22 are known.

- **CLST 1.08, item 8: Compare oxides formed on industrial analogs of Alloy 22 (Section N.4.1)**–Industrial analogs are discussed in the literature. These are reviewed in Section N.4.1. The review shows that the oxide layers of the nickel-chromium alloys consist mainly of Cr_2O_3. The thickness of the oxide film was a function of the environment and potential. The data on industrial analogs are consistent with observations of Alloy 22.

- **CLST 1.09, item 1: Characterize film stability on base metal (Section N.4.7)**–The oxide film stability on base metal is tested using two electrochemical metrics: the

corrosion rate derived from the polarization resistance and the corrosion rate derived from the final current after holding samples at fixed potential.

- **CLST 1.09, item 2: Characterize film stability on welds (Section N.4.7)**–The oxide film stability on weld samples is tested using two electrochemical metrics: the corrosion rate derived from the polarization resistance and the corrosion rate derived from the final current after holding samples at fixed potential.

- **CLST 1.09, item 3: Characterize film stability on thermally-aged materials (N.4.8)**–The oxide scale that forms on Alloy 22 during a solution annealing step was characterized using several methods. The approximately 1-μm-thick oxide is composed of layers of chromium oxide, iron oxide, and nickel oxide. The grain boundaries have a smaller polycrystalline grain structure as compared to the center of the grains. Potentiodynamic scans show that the scale does not adversely affect the corrosion performance of solution-annealed samples. Oxides that form at lower temperatures (400°C to 750°C) but longer times (years) also have a thick, predominantly chromium oxide scale like the solution-annealed substrates.

- **CLST 1.09, item 4: Titanium**–General corrosion and localized corrosion of titanium are discussed in detail in Section 10 of this technical basis document. Passive film studies on titanium are not planned based on the low general passive corrosion rates observed and the substantial margin for passive film breakdown exhibited under electrochemical testing.

The information in this report is responsive to agreements CLST 1.08 and CLST 1.09 made between the DOE and NRC. The report contains the information that DOE considers necessary for NRC review for closure of these agreements.

N.4 BASIS FOR THE RESPONSE

The issues above are addressed in an aggregate response, as they are all associated with the characteristics of the oxide film (e.g., composition, structure, mechanical properties, and stability). In this KTI response, the characterization of the oxide using several different complementary surface science techniques including atomic force microscopy (AFM), XPS, AES depth profiling, scanning electron microscopy (SEM), transmission electron microscopy (TEM), and EELS is addressed. The question of passive film stability is also addressed using electrochemical methods, which provide comparative metrics.

Most metals are thermodynamically unstable and will convert to an oxide when exposed to the environment. Despite this thermodynamic driving force, metals exist over geologic timescales. One reason for this is that as the metal is converted to metal oxide, the oxide forms a film on the surface that limits diffusion between the environment and the metal. In cases where the oxide is stable, the growth is a self-limiting process (i.e., as the film thickens, the diffusion across it slows, and the metal oxidizes at an ever-diminishing rate). In cases where the oxide is not thermodynamically stable, it is dissolving at the oxide–solution interface. As the oxide dissolves, the metal oxidizes at the metal–oxide interface. The system achieves a steady state with a particular oxide thickness when the oxide dissolution and the metal oxidation rates are

balanced. Once sufficient metal has transferred to solution, the solution becomes saturated with respect to the oxide, and the driving force for dissolution at the oxide–solution interface stops. The finding of this report is that Alloy 22 develops a chromium oxide barrier layer in the range of environments tested (NaCl and multi-ionic brines at pH values approximately 3 to 12). The oxide phases expressed are consistent with thermodynamically stable oxides in the passive region. However, given the low metal concentrations in solution (approximately 10^{-5} mol/L), it seems more likely that the oxides are kinetically stable, representing the second case. The measured short-term corrosion rates are low, suggesting that the dissolution kinetics of chromium oxides is very slow. The corrosion rates are also approximately the same in the experimental conditions tested, signifying that dissolution is not a sensitive function of pH ranging in value from approximately 3 to 12.

In this report, the oxide formation on Alloy 22 is examined as a function of two important corrosion parameters: solution pH and applied potential. Oxides were tested in solutions with pH values of approximately 3 to 12. The voltages were ranged from the open circuit potential (the potential established when the metal equilibrates with its solution environment) and the breakdown potential (the potential where the metal and oxide actively dissolve). The samples tested were Alloy 22 base metal and Alloy 22 weld metal coupons 5/8 in. in diameter and 1/8 in. thick. The coupons were polished to 0.02-μm finish, and held in the test solution vertically using a Teflon washer so only the polished face was exposed to solution. All electrochemical test data presented is referenced to a saturated Ag/AgCl electrode (0.199 V versus standard hydrogen electrode). The oxide was found to exhibit passive behavior at all voltages tested between open circuit and breakdown potentials. Near pH 3 (±0.4), the oxide is a thin (about 4 nm thick), smooth conformal layer. At higher potentials within the passive region, the oxide becomes thinner but more compact and uniform. The oxide is predominantly chromium with some molybdenum, nickel, and tungsten. At pH near 8 (±0.5), the oxide in the passive region is similar to that found in the acidic region; it is mostly chromium oxide with lower concentrations of molybdenum and nickel. At higher voltages, the oxide transforms into a thick multilayered structure with a compact oxide (about 4 nm thick) near the surface and a porous structure between 30 and 40 nm thick at the oxide–solution interface. The outer porous oxide is predominantly nickel oxide with some iron oxide. At basic pH, the surface has a coating of porous silica scale due to dissolution from the glassware. However, silica is present in a range of relevant brines and is observed to precipitate out of solution at the oxide–solution interface. The oxide underlying the silica is compact and is composed primarily of chromium oxide. In all cases, a noncrystalline chromium oxide with oxidation state 3+ is responsible for the passive behavior of the metal.

To address the question of film stability, two electrochemical metrics were used: (1) the polarization resistance and (2) the current density after holding the voltage fixed for a period of time. These were converted to a corrosion rate (or penetration rate) so they could be compared. From the polarization resistance data, it was found that the average corrosion rate was lowest in solutions near pH 8, that the welds did not differ significantly from the base metal, and that the corrosion rate did not trend with open circuit potential. The average polarization resistance corrosion rate values after 24 hours open circuit potential and their standard deviations are 2.1 ±1.2 μm/yr, 0.3 ±0.3 μm/yr, and 1.5 ±0.4 μm/yr for pH values approximately 3, 8, and 11, respectively (DTN: LL040500812251.091).

From the electrical current data, after 18 hours at fixed voltage, the primary finding was that the corrosion rate did not exhibit strong trends with either pH ranging in value from approximately 3 to 12 or with applied voltage between the open circuit and breakdown potential. In all cases, the current decayed logarithmically to the microampere range within 18 hours. It is expected that the current continues to decay logarithmically in time, and thus the corrosion rates found after 18 hours will be higher than those found at longer times. The short-time corrosion rates, then, are a metric that allows comparison between solutions and environments but the rates are several orders of magnitude higher than found in long-term testing. The average final current corrosion rate values and their standard deviations are 1.9 ±3.0, 2.0 ±1.7, and 1.9 ±1.6 μm/yr for nominal pH values of 3, 8, and 11, respectively (DTN: LL040500712251.090). Because the final current did not depend strongly on potential, the final current corrosion rates were averaged over applied voltage between the open circuit and breakdown potentials. As was found in the polarization resistance measurements, the welds and base metal did not differ significantly (DTN: LL040607412251.108).

Passive behavior was exhibited over a wide range of pH and applied voltage values. In all cases, chromium oxide in the 3+ oxidation state was the predominant oxide phase and appears to be responsible for the passivity.

Equilibrium speciation modeling suggests that there are two chromium(III) oxides that may form in the passive region: Cr_2O_3 at pH 2.8 and $NiCr_2O_4$ at pH 7.5. The experimental characterization of the oxide is consistent with these phases. However, for the oxide and solution to be in equilibrium, sufficient metal must first dissolve into solution so that the solution becomes saturated with respect to the oxide phases. In the testing performed, the solution volume is large in comparison to the metal surface area. This, in combination with the fact that Alloy 22 has a very slow dissolution rate, means that the solution metal concentrations are approximately 10^{-5} mol/L or less (the value 10^{-5} mol/L represents an upper bound approximation assuming the integrated current only represents base metal dissolution). Therefore, the oxides seen on Alloy 22 in the short-term, large solution volume tests are kinetically stable, and thus, the low corrosion rates are due to the slow dissolution kinetics of chromium(III) oxides.

It has been demonstrated that Alloy 22 creates an amorphous chromium(III) oxide barrier that isolates the metal from its environment by limiting ionic and electronic currents. The oxide phases are consistent with the equilibrium phases Cr_2O_3 and $NiCr_2O_4$. However, the metal ion concentration in solution is below the predicted equilibrium concentration. Therefore, the solution and oxide are not yet in equilibrium, and the measured corrosion rates represent the dissolution kinetics of chromium(III) oxides. This suggests that a kinetically stable chromium oxide layer forms well before enough metal dissolves into solution to make the solution saturated with respect to the oxide phase. If sufficient current were to flow, or if the solution volume were small (as might be expected in vapor or water droplets on the waste package surface), then the solution would saturate, and the oxide would become thermodynamically stable under fixed conditions. The dissolution rates are expected to become even slower as the solution–oxide system moves closer to equilibrium, and thus, the corrosion rates will decrease in time.

The technical basis for the characterization of the oxide composition and for demonstrating that the oxide shows passive behavior is given below. Section N.4.1 provides background information and theoretical predictions describing the role of pH and applied potential in oxide

formation and stability. In Sections N.4.2 to N.4.5, the oxide is characterized as a function of applied potential and pH. In Section N.4.6, the oxide growth rate is shown to be logarithmic in time. In Section N.4.7, the stability of the oxide is discussed in terms of short-term electrochemical tests.

N.4.1 Formation of Passive Films on Alloys

This section reviews the behavior of passive films on various nickel- and chromium-containing alloys. Most metals and metal alloys (with the exception of noble metals) undergo the spontaneous formation of an oxide film on the surface of the metal when exposed to oxidizing conditions such as water, air, or other oxygen containing fluids and gases (Schmuki 2002). The conversion of metal to metal-oxide consumes some of the metal and is itself a form of corrosion. Thus, the oxide film will only serve as a protective layer if the growth is a self-limiting process (i.e., the film grows to a limited thickness, creates a barrier to transport of oxygen and metal as it thickens, and then stops growing). These films, which are often less than a few nanometers thick, determine the corrosion behavior of the underlying metal or alloy (Olsson and Landolt 2003).

When a metal comes into equilibrium with a solution, some fraction of the metal atoms can become soluble solution or gas species which diffuse away from the metal surface, and some fraction can convert to a solid oxide or hydroxide that remains on the metal surface. When a voltage is applied to the metal relative to the solution, reactions that favor electron transfer are biased, and the equilibrium distribution of oxides, gasses, and solution species, are shifted. The effects of pH and potential are summarized in phase diagrams first conceptualized in *Atlas of Electrochemical Equilibria in Aqueous Solutions* (Pourbaix 1974). They are calculated from thermodynamic parameters, including energy of formation, activity of the ions in solution, pH, and potential. While equilibrium phase diagrams are useful tools, oxides formed on lab timescales may be metastable phases, and the formalism assumes that bulk oxides form. It should also be noted that Pourbaix maps (pH-potential diagrams) do not provide direct information about film structure or corrosion resistance. For this, experiments were performed to correlate oxide phases with corrosion performance.

Different metal oxides and hydroxides display different behaviors in solutions of various ionic concentrations, temperature, and pH. This variety of behaviors can be exploited by alloying the metal such that it will have components that are stable in all anticipated operating conditions. The alloying components of Alloy 22 were specifically chosen to confer passivity over a wide range of applied potential and pH values. Several models have been proposed to describe why an alloying element protects the surface. These models address various mechanisms of corrosion and can often describe the same experimental results. As a result, it is difficult to say which alloying element is responsible for a specific type of corrosion resistance behavior. Differing models place emphasis on passive film structure (Lloyd et al. 2003), percolation (Qian et al. 1990; Sieradzki and Newman 1986), charge mobility (Lin et al. 1981), and charge distribution in the film.

Based on the alloying effect, an alloy can be tailored to fit a specific set of environmental conditions by selection of constituent elements that have strengths that compensate in the areas where the other elements fail. However, because of the complex nature of passive films on

alloys, it is not always clear which element or combination of elements provides the passivity in a specific region. For Ni-Cr-Mo alloys, it is believed that the molybdenum provides resistance against reducing acidic environments; chromium against oxidizing conditions; chromium and molybdenum against localized attack; and nickel, chromium, and molybdenum against stress corrosion cracking due to chloride ions (Friend 1980).

The program EQ3/6 was used to determine the equilibrium oxide phases at two Eh and two pH points. Table N-1 summarizes the solid phases that form when 1 g of Alloy 22 is reacted with 1 kg of 1 mol/kg NaCl at 90°C. The pH values were chosen near target experimental conditions, and the voltage values are within the passive regions. At pH 2.8, these results predict that Cr_2O_3 will be the major oxide species with minor contributions from $NiWO_4$. An iron and molybdenum oxide, $Fe_2(MoO_4)_3$, should appear as the voltage is increased. Near neutral pH, nickel oxides are expected. Cr_2O_3 is undersaturated at pH 7.5, and chromium is predominantly in the spinel phase $NiCr_2O_4$. At the higher potential value, there are no thermodynamically stable chromium oxides that are expected to be in equilibrium with the solution.

Table N-1. Results From EQ3/6 Showing the Equilibrium Oxide Phases that Form when 1 g of Alloy 22 is Reacted with 1 kg of 1 mol/kg NaCl at 90°C

pH (National Bureau of Standards scale)	Potential (V)	V vs. Ag/AgCl	Mineral	Formula	Moles
2.8	0.22	0	Eskolaite	Cr_2O_3	2.10×10^{-3}
				$NiWO_4$	1.63×10^{-4}
2.8	0.57	0.35	Eskolaite	Cr_2O_3	2.10×10^{-3}
				$Fe_2(MoO_4)_3$	2.65×10^{-4}
				$NiWO_4$	1.63×10^{-4}
7.5	-0.09	-0.31	Bunsenite	NiO	7.42×10^{-3}
				$NiCr_2O_4$	1.69×10^{-3}
				$CoCr_2O_4$	4.24×10^{-4}
			Trevorite	$NiFe_2O_4$	2.69×10^{-4}
				$NiWO_4$	1.53×10^{-4}
7.5	0.49	0.27	Bunsenite	NiO	9.11×10^{-3}
			Trevorite	$NiFe_2O_4$	2.69×10^{-4}
				$NiWO_4$	1.52×10^{-4}
				Spinel-Co	1.41×10^{-4}
				MnO_2 (gamma)	9.10×10^{-5}

Source: DTN: LL040502712342.006.

These calculations give the equilibrium oxide phases with a relatively high concentration of metal in the solution (approximately 0.01 mol/L). In the experiments discussed, the metal solution concentrations are several orders of magnitude smaller (approximately 10^{-5} mol/L) due to the slow dissolution rate of Alloy 22 and the large solution volumes used. It is, therefore, expected that the measured oxides are likely to be undersaturated with respect to the solution phase and represent kinetically stable phases rather than thermodynamically stable phases. Nevertheless, as will be seen in upcoming sections, the kinetically formed film has oxide phases that are consistent with those expected to evolve in equilibrium.

Literature Survey of Oxide Formation–This section reviews the properties of the passive oxide films of several nickel- and chromium-containing industrial analogs of Alloy 22. In most cases, systems exposed to similar environments as the present study are highlighted (i.e., aqueous NaCl solutions in various pH buffers and at various potentials).

Nickel-Based Alloys–There are a considerable number of commercial Ni-Cr and Ni-Cr-Fe alloys (Piron et al. 1969). For example, Inconel 600 is a well-known Ni-Cr-Fe alloy. Inconel 600 is used in place of Ni 200 when a higher strength material is required or moderately sulfurizing conditions are present. Additionally, Inconel 600 is used extensively in the steam generators of pressurized water reactors in the nuclear industry.

Ni-Cr-Mo alloys exhibit excellent corrosion resistance in both oxidizing and reducing environments and are considered the most corrosion resistant of the nickel-based super alloys. Consequently, many of these alloys are used in industrial applications. Some well-known industrially applied alloys include Hastelloy C-4, Hastelloy X, Hastelloy C-276, and Inconel 625. An excellent review of the corrosion resistance properties of each is detailed in the literature (Friend 1980).

The addition of molybdenum to nickel-based alloys has been shown to decrease corrosion rates with increasing molybdenum content. Several plausible explanations for the mechanisms responsible for increased corrosion resistance with increased molybdenum content have been developed. Among these, it has been proposed that a primary function of molybdenum is to retard the propagation of localized corrosion once the passive film breakdown has occurred. It has been postulated that molybdenum preferentially locates at local defects on the surface, which otherwise would act as dissolution sites (Lloyd et al. 2003).

Chemical Composition–XPS measurements have been utilized to study the chemical composition of the passive films of several Ni-Cr alloys after 24-hour immersion in 0.1 mol/L NaCl (Lim and Atrens 1992). XPS analyses showed that, for each Ni-Cr alloy, the oxide film contained only Cr_2O_3. Electrochemical techniques were used for the determination of the relative corrosion rate of the alloys. The results showed that Ni-Cr10 and Ni-Cr20 alloys showed a slightly higher corrosion rate than Ni-Cr40.

Jabs et al. (1997), using XPS, have studied the chemical compositions of passive films of Ni-Cr alloys in both basic (1 mol/L NaOH) and acidic (0.5 mol/L H_2SO_4) environments. In NaOH solutions, the thickness and composition of the passive layer as a function of passivation potential was characterized. The passive film of Ni-Cr20 in both 0.5 mol/L H_2SO_4 and 1 mol/L NaOH, was a bilayer with an oxide interfacial layer and a hydroxide layer above it. In 1 mol/L NaOH, nickel is enriched at the metal surface and forms the outer hydroxide layer, especially at positive potentials and for long passivation times. The oxide layer consisted mainly of Cr_2O_3. NiO was also present in the passive film but entered only in the transpassive potential region (greater than 600 mV versus standard hydrogen electrode). The thickness of the passive film increased linearly with potential (from 1 nm at –500 mV versus standard hydrogen electrode to 5 nm at 600 mV versus standard hydrogen electrode). In acidic solutions (0.5 mol/L H_2SO_4), the oxide and the hydroxide part of the passive film contained only chromium(III) ions with minor evidence of nickel(II) and chromium(VI) in the transpassive range. The passive film thickness for acidic solutions was a linear function of the potential. The thickness of the passive film

increased linearly with potential from 0.5 nm at −500 mV versus standard hydrogen electrode to 3 nm at 600 mV versus standard hydrogen electrode. The fact that the passive oxide film is thicker in basic solutions has also been observed in stainless steel alloys (Schmutz and Landolt 1999).

Marcus and Grimal (1992), using XPS, characterized the passive film of Ni-Cr-Fe alloys that closely resemble Inconel 600 in dilute acidic solution (0.05 mol/L H_2SO_4). XPS analyses of passive layers formed on Ni-Cr21-Fe8 at 300 mV versus standard hydrogen electrode and 600 mV versus standard hydrogen electrode demonstrated the existence of a bilayer structure. The inner oxide layer consisted of approximately 96% Cr_2O_3 and 4% Fe_2O_3. There was no detectable nickel(II). The outer hydroxide layer was approximately 100% $Cr(OH)_3$. At 300 mV versus standard hydrogen electrode, the thickness of the passive film was 1.1 nm, and the thickness of the inner oxide layer was 0.65 nm. At 600 mV versus standard hydrogen electrode, the film was thicker (the thickness of the inner oxide layer was 0.9 nm).

The passive film for Hastelloy Alloy C-276 and Alloy 22 in 1 mol/L NaCl + 0.1 mol/L H_2SO_4 has been characterized using XPS for chemical composition and time of flight secondary ion mass spectroscopy (TOF-SIMS) for passive film thickness (Lloyd et al. 2003). The passive film on Alloy 22 exhibits a bilayer structure. TOF-SIMS analyses show a layered oxide structure consisting of a Mo/Cr oxide-rich outer layer and Cr/Ni oxide-rich inner layer. Although the bilayer persists at potentials ranging from 200 mV to 700 mV versus Ag/AgCl, the concentration percentages of the oxides in the two layers were a function of potential. In general, the overall chromium content increased steadily, and the nickel content decreased with increasing potential. The increase in chromium content was predominantly within the inner regions of the film. Based on XPS results, the oxidation states in the passive film were NiO, Cr_2O_3, and MoO_3. It is important to note that there was no evidence of chromium(VI) within the oxide film, indicating that oxidative dissolution leads to the release of all chromium(VI) species formed to the solution. By contrast, molybdenum(VI) was retained as the dominant species in the oxide at higher potentials.

Oxide thicknesses increased linearly with potential (Lloyd et al. 2003). The thicknesses, determined by TOF-SIMS analyses, were measured to be 2.0 nm at 200 mV, 2.3 nm at 500 mV, and 2.8 nm at 700 mV versus Ag/AgCl. In general, the oxide thicknesses on Alloy 22 are similar to those mentioned above for Ni-Cr alloys (Jabs et al. 1997).

The passive film of Alloy 276 does not show as clear a bilayer structure as Alloy 22, but it does contain the same constituents. The chromium content of the oxide was lower on C-276 than Alloy 22 and only increased significantly after the potential was raised into the transpassive region (greater than 700 mV versus Ag/AgCl). The overall molybdenum content of the oxide on C-276 was significantly higher than on Alloy 22. Lloyd et al. (2003) commented that the inability of C-276 to retain chromium within a barrier layer at the alloy–oxide interface may explain the greater sensitivity to localized corrosion as the temperature increases for C-276.

Film Stability–Hodge and Wilde (1970), using anodic polarization techniques in 0.5 mol/L H_2SO_4 + 1 mol/L NaCl at 25°C, found that Ni-Cr alloys containing more than 10% chromium develop passivity and are resistant to dilute sulfuric acid solutions containing certain amounts of chloride. A similar effect of the addition of chromium to nickel was shown by Piron et al. with a

potentiostatic anodic polarization study of Ni 200 and Inconel 600 in 0.5 mol/L H_2SO_4 solutions at 24°C, to which was added sodium chloride in various amounts from 0 to 3.5 wt % (Piron et al. 1969). A quantitative measure of the effect of chloride ions on the passivity of those two materials in 0.5 mol/L H_2SO_4 was achieved by maintaining the potential of each electrode within the passive region (+600 mV versus standard hydrogen electrode in the case of Inconel and +500 mV versus standard hydrogen electrode in the case of nickel). Subsequently, the concentration of chloride ions was increased by the addition of increments of a concentrated sodium chloride solution. At each concentration, the steady state passive current density was measured. The results showed that, for each material, the breakdown of passivity occurred at a critical NaCl concentration (Friend 1980).

The stability of the passive films of several Ni-Cr-Mo alloys has been discussed in detail (Friend 1980). In summary, Alloys C, C-276, C-4, and Inconel alloy 625 have been tested for corrosion resistance in titrated acidic solutions, including HCl, H_2SO_4, HNO_3, HF, and HPO_3. The alloys with higher molybdenum content usually show the best resistance to reducing environments such as H_2SO_4 and HCl and pitting attacks from chloride-containing solutions, while the alloys with higher chromium content usually have the best resistance to strongly oxidizing solutions such as nitric acid (Friend 1980).

N.4.2 Experimental Determination of the Oxide as a Function of pH and Applied Potential

To determine the oxide phases responsible for passive behavior, oxide films were grown on Alloy 22 at several pH and applied potential values. Specimens were tested in complex multi-ionic solutions that were based on concentrated repository groundwaters (see Orme 2003a, Orme 2003b, and Orme 2004 for solution compositions). These solutions are referred to as simulated acidic water, (SAW), simulated concentrated water (SCW), and basic saturated water (BSW). In addition, simplified, buffered solutions were used to allow a better comparison with theoretical models and literature. This work focuses on three pH values with nominal values 3, 8, and 11; these solutions are designated “pH3,” “pH8,” and “pH11,” respectively (but only electrochemical tests were conducted at pH 11). The pH values cited are approximate.

The voltages were chosen by examining the anodic polarization curves. These current-voltage plots are shown in Figure N-1 for the buffered 1-mol/L NaCl solution and in Figure N-2 for the multi-ionic solutions. It should be noted that the curves at similar pH levels are almost identical for the simplified and multi-ionic solutions. The observation that the current-voltage curves are a function of pH, independent of the ionic species found in repository solutions, removes one level of complexity from the problem of determining the oxide film in all relevant repository conditions.

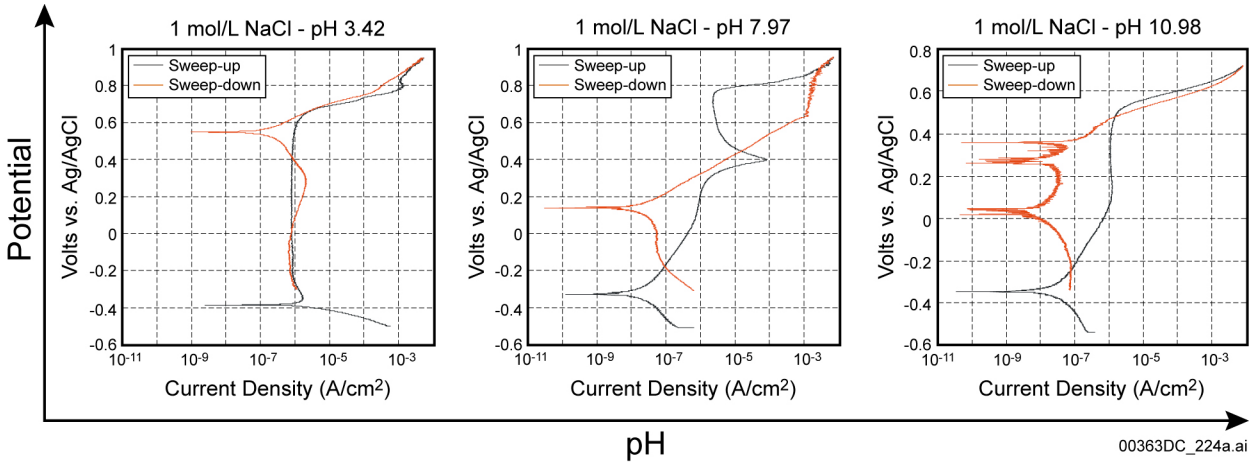

Source: DTN: LL040505512251.101.

NOTE: Curves are shown for pH values of 3.42 (DEA 569), 7.97 (DEA 568), and 10.98 (DEA 1102). The forward (anodic) voltage scan is shown in black, and the reverse cathodic voltage scan is shown in red.

Figure N-1. Potentiodynamic Scans of Alloy 22 in Buffered 1-mol/L NaCl Solutions

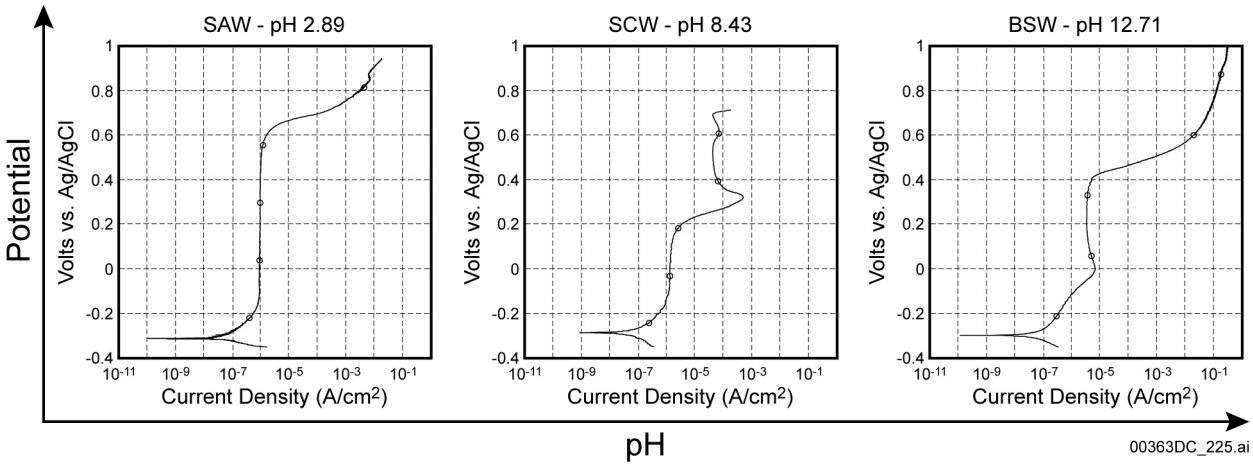

Source: DTNs: LL040505512251.101.

NOTE: Curves are shown for pH values of 2.89 (DEA 492), 8.43 (DEA 1246), and 12.71 (DEA 461). The electrochemical response is almost identical to the simpler 1-mol/L NaCl solutions at similar pH values.

Figure N-2. Potentiodynamic Scans of Alloy 22 in Simulated Acidified Water, Simulated Concentrated Water, and Basic Saturated Water Solutions

To characterize the oxide, films were grown potentiostatically at several voltages between the open circuit potential and the onset of transpassive dissolution. Figures N-1 and N-2 are organized according to increasing pH to suggest that changes in the current response may indicate a phase transition in the oxide film. As the voltage is varied, phase boundaries are traversed, and different oxide phases become stable. These transitions will affect the current response of the system. Phase changes usually involve dissolution and the flow of metal or oxygen ions (i.e., when a phase transition occurs, current flows). Constant current plateaus, such as seen between −300 mV and 600 mV in the pH 3 solution, suggest that this entire region has a

similar oxide composition. In contrast, in solutions near pH 8, the two regions above and below the anodic peak at approximately 400 mV are likely different oxides. While this is not a rigorous analogy, these observations suggested regions in pH-potential space and these were chosen for more detailed investigations. Table N-2 contains a summary of the samples, test conditions, and analysis methods discussed in this section. The three pH regions will be discussed in turn.

Table N-2. Summary of Oxide Growth Conditions and Analysis Shown in this Section

Metal Alloy	Solution	pH	Sample ID	Voltage versus Ag/AgCl (mV)	Temperature (°C)	Analysis
Alloy 22	pH3	2.72	DEA 565	200	90	XPS, AES
Alloy 22	pH3	2.68	DEA 562	200	90	TEM, AFM
Alloy 22	pH3	2.87	DEA 567	500	90	TEM
Alloy 22	pH3	2.70	DEA 566	500	90	XPS, AES, AFM
Alloy 22	SAW	2.98	DEA 495	400	90	XPS
Alloy 22 Weld	pH3	3.38	JE 3022	200	90	XPS
Alloy 22 Weld	pH3	3.39	JE 3025	400	90	XPS
Alloy 22	pH8	8.12	DEA 543	200	90	TEM
Alloy 22	pH8	8.11	DEA 539	200	90	XPS, AES
Alloy 22	pH8	7.56	DEA 557	400	90	TEM
Alloy 22	pH8	8.03	DEA 518	200	90	AFM
Alloy 22	pH8	8.07	DEA 532	400	90	AFM
Alloy 22	pH8	7.56	DEA 556	400	90	XPS, AES
Alloy 22	pH8	8.03	DEA 520	650	90	TEM
Alloy 22	pH8	7.66	DEA 559	650	90	XPS, AES, AFM
Alloy 22	BSW	12.48	DEA 465	250	90	XPS
Alloy 22	BSW	12.76	DEA 496	250	90	TEM

Source: DTNs: LL040206712251.074, LL040206412251.071, LL040207512251.076, LL040207612251.077, LL040206612251.073, LL040308412251.081, LL040206512251.072, and LL040500512251.088.

NOTE: The pH value labels in the solution column are used as solution designations, representing the approximate solution pH value.

N.4.3 Experimental Evaluation of the Oxide that Forms under Acidic Conditions

Alloy 22 specimens were tested in solutions near pH 3. From the cyclic polarization curve in Figure N-1, it can be seen that the curve has classic passive behavior with a broad, approximately 1 V flat plateau region where the current is independent of the applied potential. Two potentials at either end of the passive plateau were chosen to potentiostatically grow an oxide film. The oxides were then characterized using AFM, TEM, XPS, and AES depth profiling. The oxide films formed in two acidic solutions: multi-ionic and NaCl, which are shown to be very similar.

Oxide Formed in 1 mol/L NaCl Buffered near pH 3–A 1-mol/L NaCl solution buffered near pH 3 using phthalate was used to mimic SAW under simplified (and buffered) solution conditions. The solution pH stayed constant within 0.1 pH units during the course of any given experiment but varied more widely between experiments. Experiments with pH values 3 ±0.4 have similar behavior and are grouped together in this analysis.

The AFM images are topographic maps of the surface morphology. The surface morphologies for films grown at 500 mV and 200 mV versus Ag/AgCl are shown in Figure N-3a and N-3b, respectively. The images show a smooth surface with a filamentary deposit. The filamentary surface morphology has been attributed to the phthalate buffering agent because samples exposed to SAW (also near pH 3) do not show these deposits. The surface morphology after oxide growth seen in the AFM images of Figure N-3 is similar to the surface morphology of the sample before the oxide was grown (image not shown), indicating that the oxide film is smooth and conformal to the metal surface.

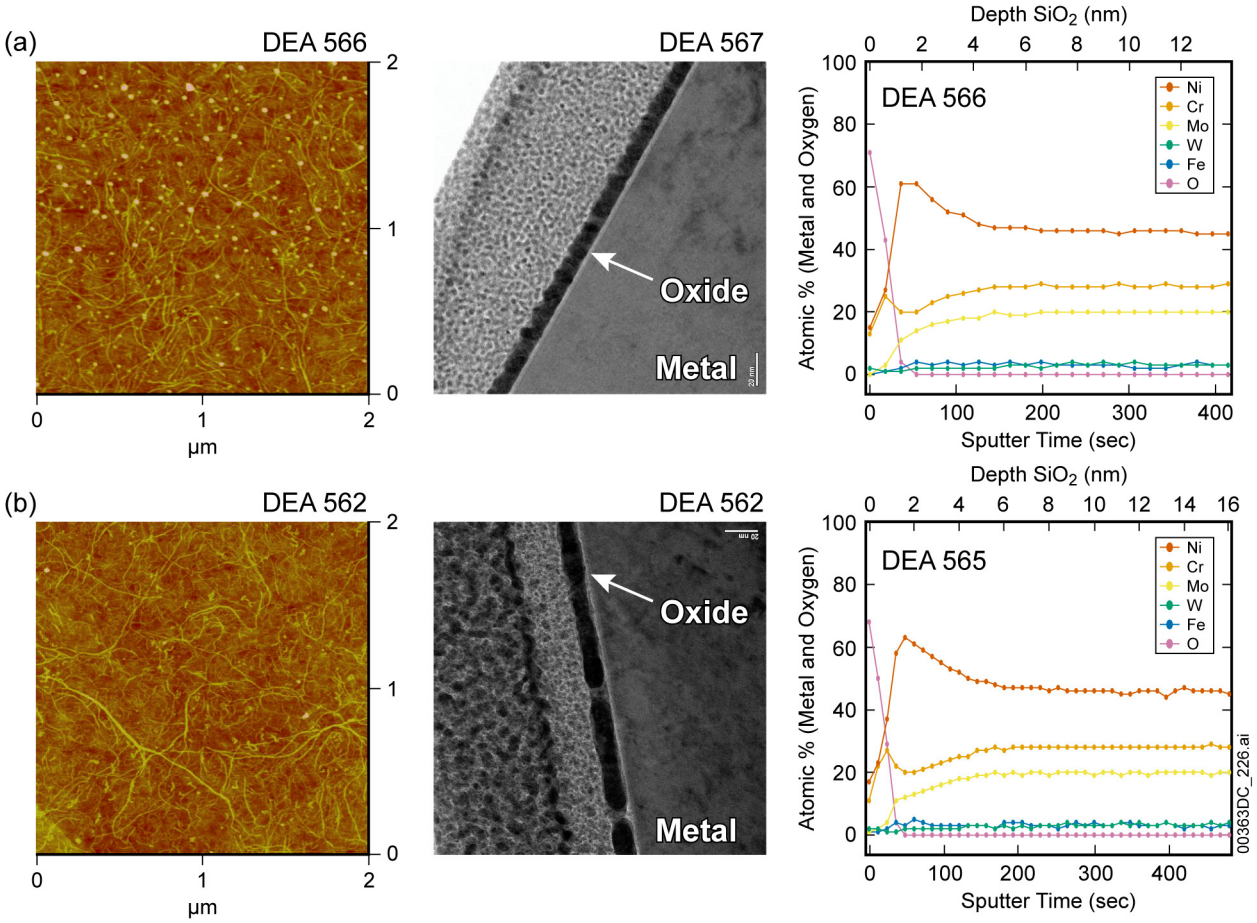

NOTE: All voltages are versus a saturated Ag/AgCl reference electrode. The first column shows AFM images of the surface morphology (DTN: LL040206412251.071). The images are 2 μm by 2 μm and have a RMS surface roughness less than 1 nm. The second column shows a cross-sectional TEM image (DTN: LL040500512251.088). The metal is on the right-hand side. The third column is AES depth profiling showing atomic composition across the oxide and into the metal (DTN: LL040206512251.072).

Figure N-3. Surface Morphology and Cross-Sectional Views of Oxides Formed at (a) 500 mV and (b) 200 mV in 1-mol/L NaCl Solution Buffered at pH 2.7

Cross-sectional TEM images show the morphology of the oxide in a cross-sectional view and allow a direct measure of its thickness. The pluck-out samples are approximately 3 μm long, and the oxide was imaged over the full length. Figure N-3 shows representative sections at 65,000X magnification. At both voltages within the passive region, a thin conformal layer can be seen at the metal surface. At the lower potential (200 mV versus Ag/AgCl), the oxide is 4.0 ±0.5 nm

and is less uniform in thickness than the 2.4 ±0.3 nm film formed at the higher voltage (500 mV versus Ag/AgCl) (DTN: LL040500912251.092).

EELS images (Figure N-4) show a definitive chromium and oxygen signal in the oxide region. The elemental maps are inconclusive regarding the presence of nickel in the oxide layer because the high concentration of nickel in the base metal makes the nickel difficult to see. In the chromium map, Figure N-4a, there is a darker line at the metal–oxide interface indicating that this area has less chromium. This is consistent with nickel enrichment at the metal surface.

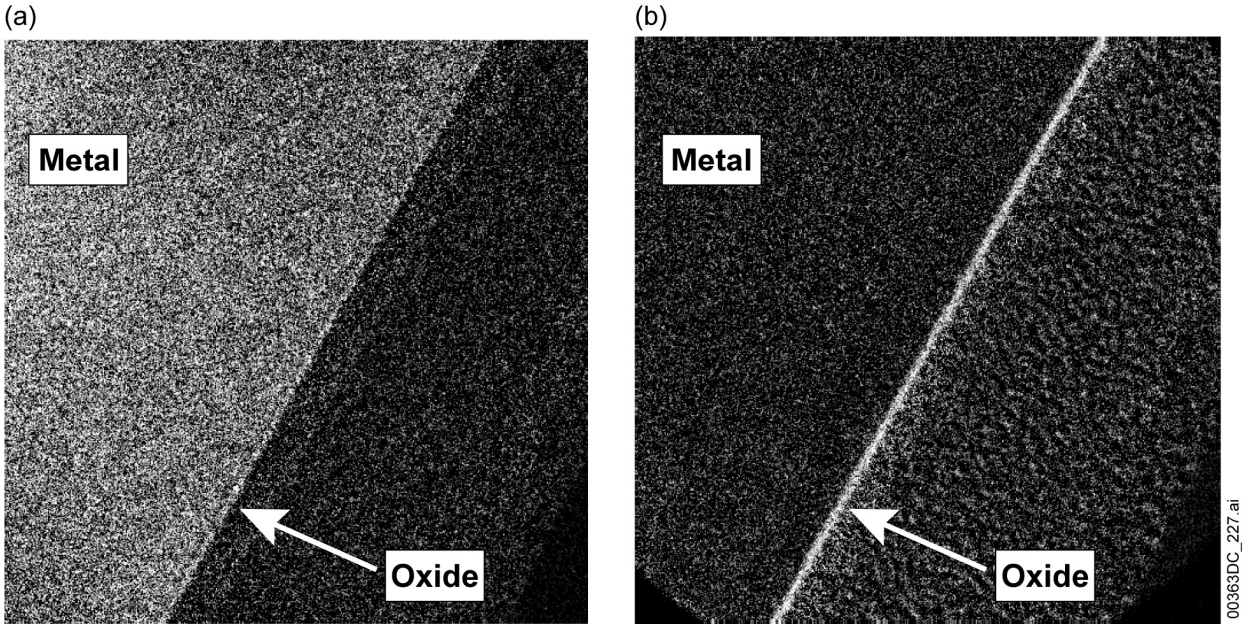

Source: DTN: LL040500512251.088.

NOTE: The maps indicate a chromium oxide barrier layer.

Figure N-4. Electron Energy-Loss Spectroscopy Showing Elemental Maps of (a) Chromium and (b) Oxygen for Sample DEA567

XPS can help determine the oxidation state of the elements. In Figure N-5, spectra for nickel, chromium, molybdenum, tungsten, iron, and oxygen are shown. The carbon peak is referenced to 284.8 eV. Because the oxide is relatively thin, the underlying metallic component (indicated on the figure as the metallic peak) is apparent for all Alloy 22 species. Because Alloy 22 base metal and Alloy 22 weld specimens have very similar electrochemical responses, XPS spectra, and oxide thicknesses, these samples have been grouped together to determine trends. Table N-3 summarizes the speciation of the chromium and molybdenum spectra. As can be seen from Table N-3, both the molybdenum and chromium spectra indicate more metallic component at lower potentials. This would typically be associated with a thinner oxide layer (which allows the electrons initiating from the metal to escape), but from the TEM cross-sectional images it is known that the oxide is thicker on average at the lower potentials. It may be that the oxide is less dense or that the oxide is less uniform at the lower potential. At the higher applied voltage levels, the NiO peak increases relative to the metallic nickel peak and the chromium speciation shifts to a higher percentage of chromium in the 3+ state (as in Cr_2O_3).

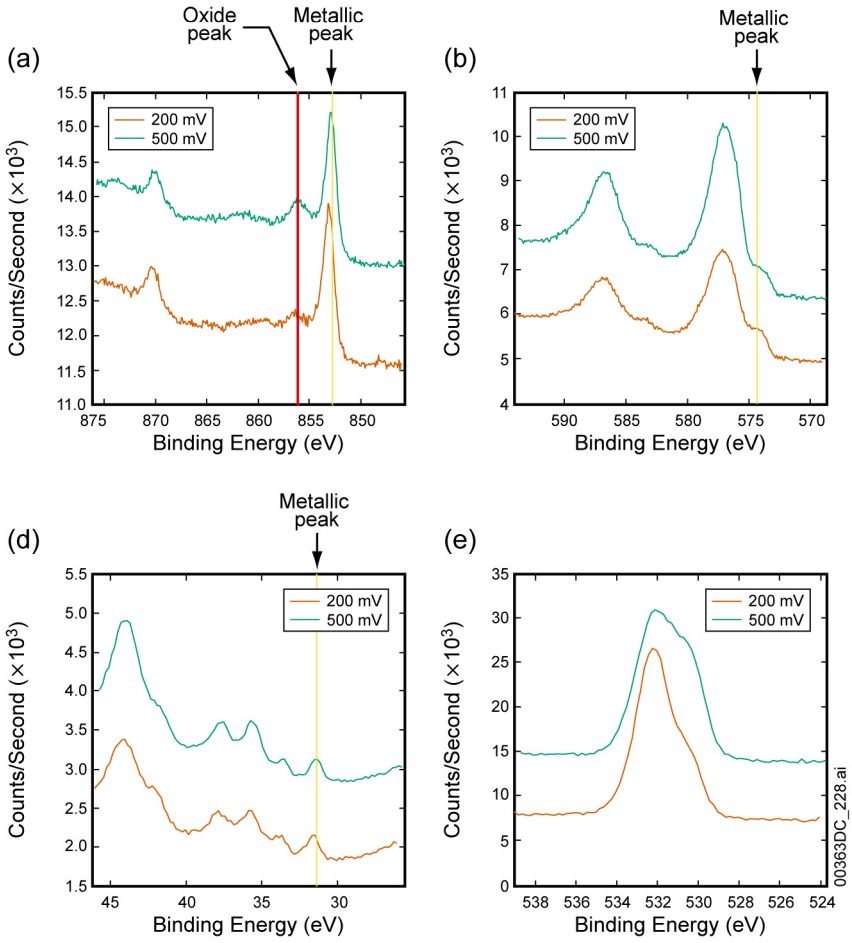

Source: DTN: LL040206712251.074; LLNL 2003a.

NOTE: The elemental regions are: (a) nickel, (b) chromium, (c) molybdenum, (d) tungsten, and (e) oxygen. For clarity, the spectra have been offset so that they do not overlay one another. Thus, the y-axis scaling is the same for each spectrum, but the y-axis zero is not always the same.

Figure N-5. XPS Spectra of Samples Held at 200 mV (DEA565) and 500 mV (DEA566)

Table N-3. Relative Speciation of Oxides, as Determined by Fitting the High-Resolution Spectra

Sample ID	Potential (mV vs. Ag/AgCl)	Auger Sputter Time (s)	Chromium (%)				Molybdenum (%)			
			Cr metal	CrO_2	Cr_2O_3, $Cr(OH)_3$, CrOOH	CrO_3	Mo Metal	MoO_2	Mo_2O_3 Hydroxide	MoO_3, Molybdate
DEA565	200	30	9.9	24.1	51.6	14.4	28.5	20	29	22.5
JE3022	200	27	8.8	18.4	54.4	18.4	33.8	16.8	17.2	32.2
JE3025	400	30	5	13	62.4	19.6	21.3	10	32.3	36.5
DEA566	500	27	5.7	17.2	60.8	16.2	22.7	11.9	32.7	32.8

Source: LLNL 2003a.

NOTE: The peaks have a large degree of overlap, and the fits may not be unique. The samples DEA565 and DEA566 are Alloy 22 base metal specimens, whereas JE3022 and JE3025 are weld specimens. The second column describes the test conditions.

Oxide Formed in Multi-ionic SAW Solution with pH 2.8–The oxide films that form in SAW solution are very similar to those formed in 1 mol/L NaCl buffered at pH 2.8 using phthalate. Figure N-6a shows a cross-sectional view of an oxide formed by 16 hours of holding in SAW at a potential 200 mV versus Ag/AgCl. Figure N-6b shows the XPS sputter profile. The TEM image shows a conformal oxide that measures 2.9 ±0.3 nm thick (DTN: LL040500912251.092). The XPS depth profile across the oxide reveals that oxide is almost entirely chromium oxide.

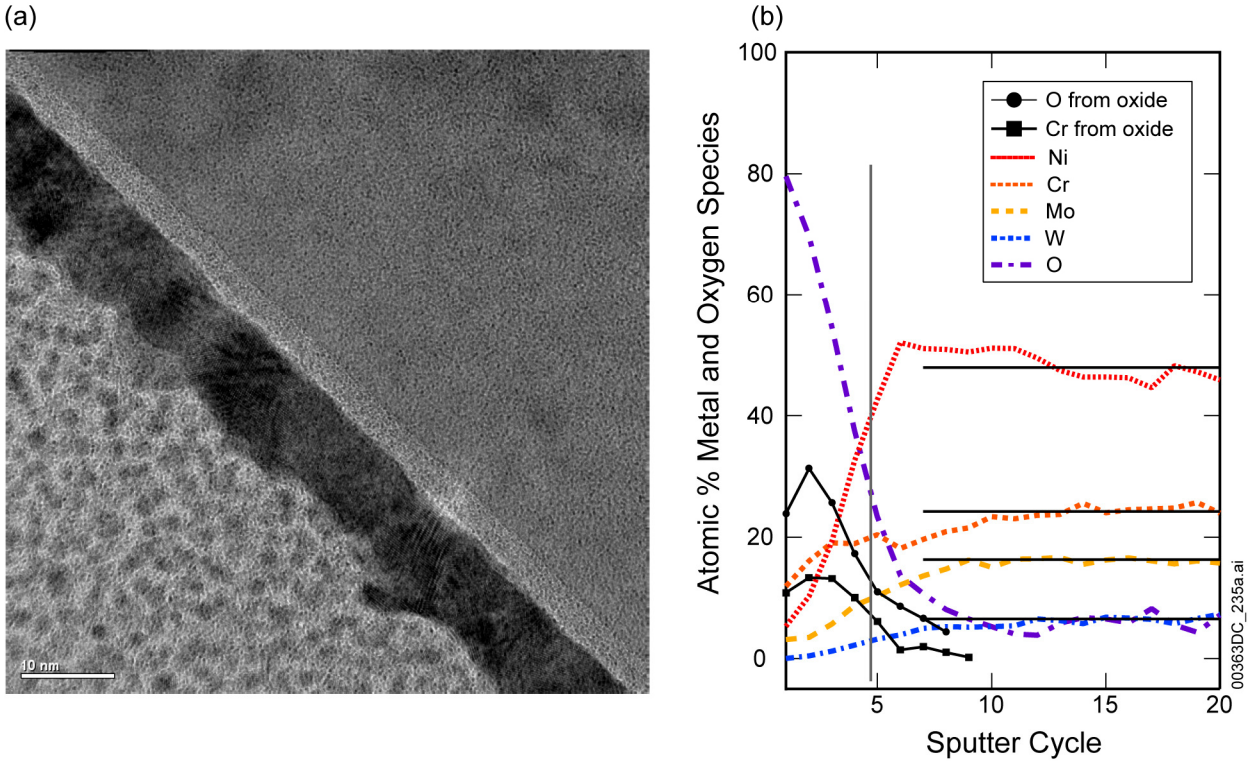

Source: (a) DTN: LL040308412251.081; (b) DTN: LL040501212251.095.

NOTE: In the depth profile, a vertical line marks the approximate location of the metal–oxide interface as determined from the half maximum value for the chromium oxide concentration. Horizontal lines mark the average values of the nickel, chromium, molybdenum, and tungsten atomic % averaged over sputtering cycles 10-36 (data were obtained for a longer duration than is presented in this graph).

Figure N-6. (a) TEM of Sample DEA495 and (b) XPS Depth Profiling of Sample DEA495, Showing the Oxide Film that Forms in the Passive Region in Acidic Solutions

The XPS sputtering profile shows the total atomic percent of nickel, chromium, molybdenum, tungsten, and oxygen. (Iron is not shown because the concentrations are low and the peaks interfere with nickel Auger lines.) The electron escape depths for the metallic elements are approximately 3 nm, which are comparable to the oxide thicknesses. For this reason, the surface oxide spectra also show a metallic component. To account for the metal contribution in the oxide spectra, metal peak fits were performed within the base metal to obtain the positions and line shapes of the metallic components. Spectra within the oxide region were then fit with a combination of metallic and oxide peaks.

Only the chromium spectra showed distinctive oxide peaks. This allowed the chromium oxide contribution to be separated from the metallic contribution in the atomic percent calculations. Both the total chromium as well as the chromium oxide are shown in Figure N-6.

The oxygen signal is partially from the oxide and partially from surface contamination. To separate these contributions, the oxygen spectra were fit with two peaks at 530 and 531 eV. The peak at 530 eV is consistent with Cr_2O_3. The oxide oxygen fraction is also shown plotted in the depth profile.

The nickel spectra are almost entirely metallic. Only one spectrum (at cycle 3) close to the metal–oxide boundary shows a slight broadening that may indicate a thin nickel oxide. This was observed for only one cycle, and because the signal to noise is low in this region, the data are inconclusive. The metallic nickel at the metal–oxide interface shows a slight increase in concentration over its average value deeper in the bulk. In the metal–oxide interface region, the other metals have not yet reached their average bulk values, whereas nickel has overshot its average bulk concentration. This nickel enhancement has been observed on several other systems and is associated with passivity.

In summary, the oxide film that forms in the passive region in SAW solution is a conformal, 2.9-nm-thick chromium oxide film consistent with chromium in the chromium(III) oxidation state. In the literature, it is found that the chromium oxide is hydrated at the oxide–solution interface and less hydrated at the oxide–metal interface; this is often referred to as a bilayer (Marcus and Grimal 1992). The signal-to-noise levels of these data were not high enough to fit the hydration peak with confidence. With the signal-to-noise levels of these data, no nickel, molybdenum, or tungsten oxides could be identified in the oxide layer. There is an enhancement of nickel metal at the interface between the oxide and the metal substrate.

N.4.4 Experimental Evaluation of the Oxide that Forms near Neutral Conditions

Oxide Formed in 1-mol/L NaCl Solution Buffered at pH 7.5–The surface oxide that forms in near neutral solution has two very distinct regions: one associated with a thin oxide similar to other passive films and another associated with a thick porous oxide. These two regions are suggested from the cyclic polarization curve in Figure N-1, which shows two constant current plateaus separated by an anodic peak at 400 mV. The first plateau, between 0 and 300 mV is associated with passive film formation. The second plateau, between 500 and 800 mV suggests that another stable oxide phase forms. The anodic peak is indicative of the formation of a second stable oxide phase. The morphology and elemental compositions of the oxide films formed at increasing voltage are summarized in Figure N-7. While the cyclic polarization showed two current regions, all potentiostatically held samples had current densities between 50 and 1,100 nA/cm^2 after 16 to 20 hours (DTNs: LL040206612251.073, LL040207512251.076 (raw data files), LL040500712251.090 (summary table)). The final currents were independent of voltage until the transpassive region near 750 mV.

Figure N-7 shows the transition in oxide as the applied potential is increased from the passive region at the bottom of Figure N-7c to a voltage near transpassive dissolution shown in Figure N-7a. Comparison with Figure N-1 shows that these correspond to the two plateaus observed in the cyclic polarization curve.

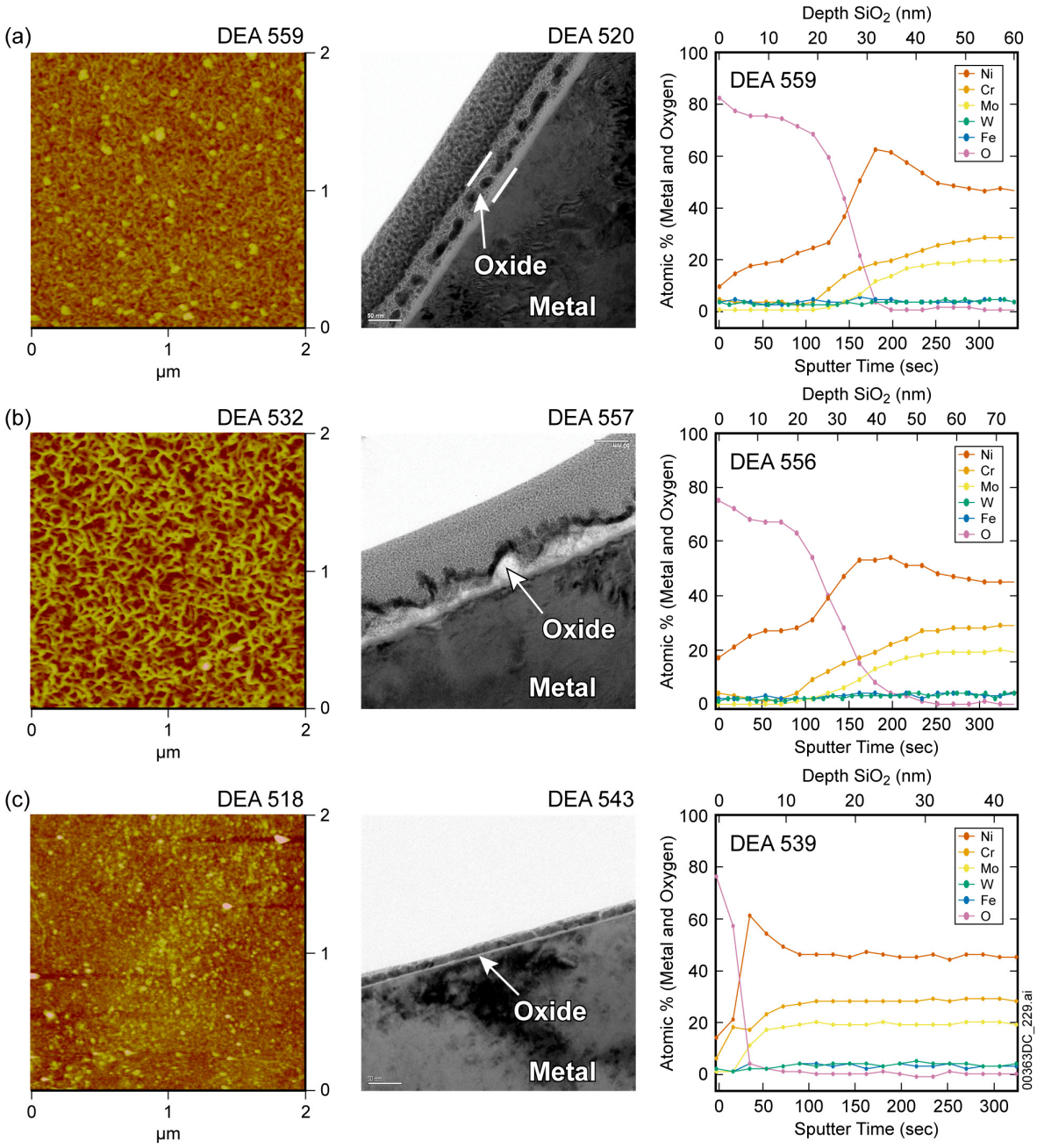

NOTE: All voltages are versus a saturated Ag/AgCl reference electrode. The first column shows AFM images of the surface morphology (DTN: LL040206412251.071); The images are 2 µm by 2 µm. The second column shows a cross-sectional TEM image (DTN: LL040500512251.088). The metal is on the bottom half of the image. In the third column, AES depth profiling gives atomic composition across the oxide and into the metal (DTN: LL040206512251.072).

Figure N-7. Surface Morphology and Cross-Sectional TEM Views of Oxides Formed at (a) 650 mV, (b) 400 mV, and (c) 200 mV in 1-mol/L NaCl Solution Buffered at pH 7.5

In the passive region, a thin, smooth oxide is observed. From the AFM images, the surface roughness is approximately the same (less than 1 nm for the 2 µm by 2 µm area) before and after oxide growth. The Auger elemental depth profile in the third column shows that oxygen, nickel,

and chromium have the highest concentrations in the oxide region. AES does not distinguish between elements in the metallic and oxide states, and most of the nickel signal is from the underlying metal substrate. Some of the chromium signal is also coming from the underlying metal, but the fact that the concentration peaks in the oxide demonstrates that there is chromium in the oxide region. There is a dip in the chromium concentration and a peak in the nickel signal at approximately the same depth. This is consistent with nickel enrichment in the metal.

Above approximately 300 to 350 mV, a thick, porous oxide forms, changing the morphology and surface roughness dramatically. From the AFM, images it can be seen that the oxide has a tighter pore structure at 650 mV than at 400 mV. The TEM images in the second column show two distinct layers in the oxide, with a compact thin layer (about 4 nm thick) close to the oxide and the porous (30- to 40-nm-thick) structure farther away. At 400 mV, the porous structure is irregular and open. The higher voltage has a finer pore size and a more uniform thickness. The distinction between the porous layer and the compact oxide is more apparent, and there appear to be voids that segregate at the compact, porous interface.

Figure N-8 shows the XPS spectra for the Cr2p, Mo3d, and Ni2p energy intervals. The film formed at 200 mV (in the passive region) demonstrates that the oxide is predominantly chromium oxide (consistent with Cr_2O_3), with some molybdenum and nickel oxide. The surfaces of the two porous oxides are predominantly nickel oxide.

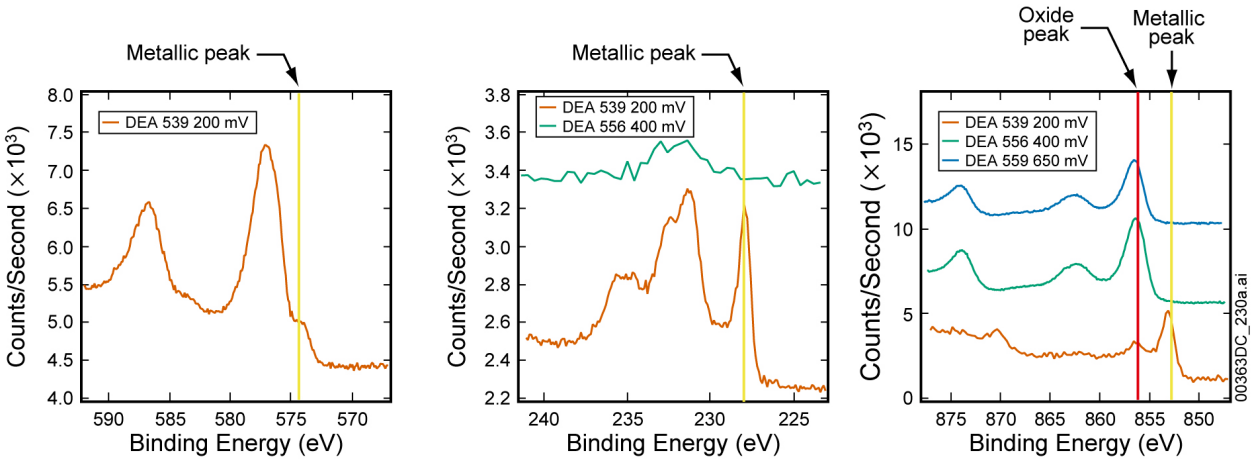

Source: LLNL 2003b.

NOTE: The figures show the Cr2p, Mo3d, and Ni2p regions from left to right. These spectra show that the surface oxide changes from a predominantly Cr_2O_3 film to a NiO as the voltage is increased from 200 to 400 mV. For clarity, the spectra have been offset so that they do not overlay one another. Thus, the y-axis scaling is the same for each spectrum, but the y-axis zero is not always the same.

Figure N-8. XPS Spectra of Samples Held at Various Voltages in pH 8 Solution

N.4.5 Experimental Evaluation of the Oxide that Forms under Basic Conditions

To determine the character of the oxide exposed to a basic solution, several samples were held potentiostatically in the passive region at 250 mV in BSW for 16 to 20 hours at a temperature of 90°C. An image of the oxide is shown in Figure N-9. The oxide has a compact layer close to the metal and a porous outer layer. In basic solution (pH of approximately 12.5), the glass electrochemical cell partially dissolves, adding silica to the solution. The porous region is likely a silica deposit from the glassware. This was especially apparent when examining samples tested in simple NaCl/NaOH solution. The dissolved glassware formed thick silica deposits on the sample surface, precluding any surface characterization. Silica surface deposits are also observed on Alloy 22 specimens exposed in the LTCTF to silica-containing waters.

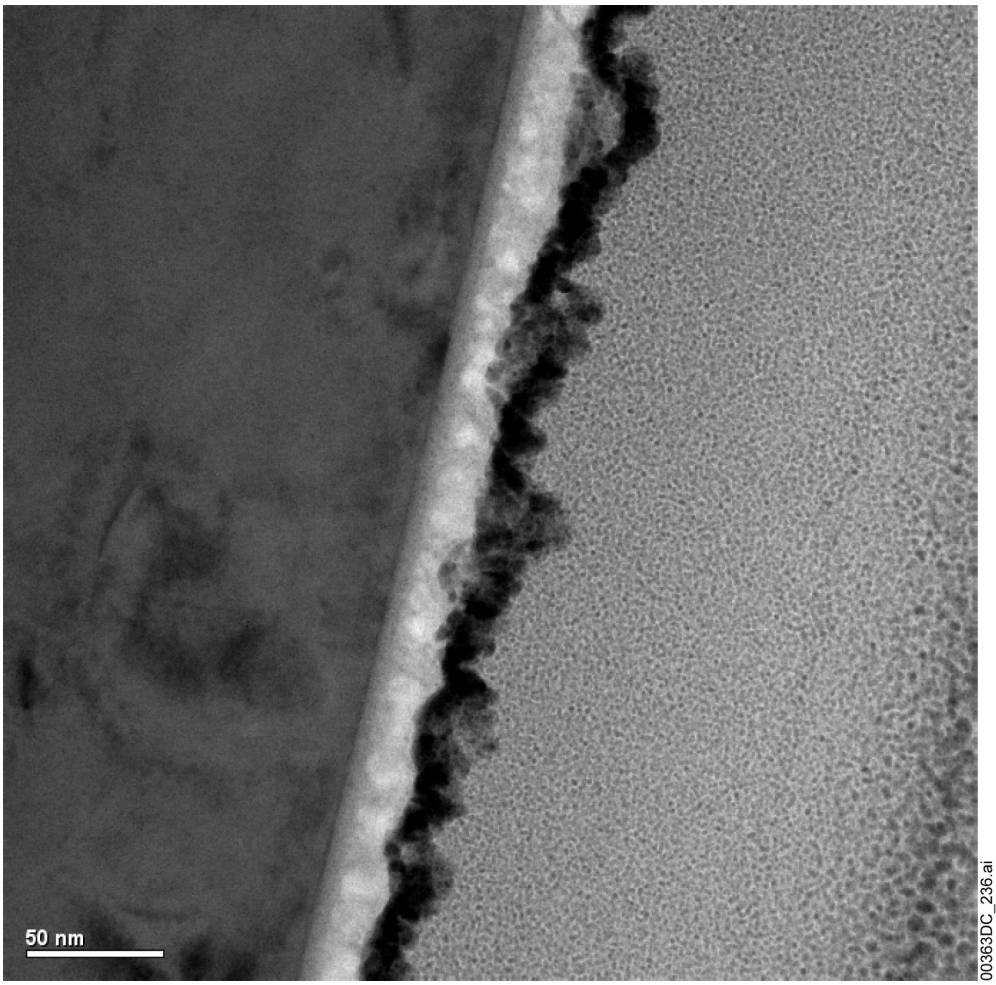

Source: DTN: LL040308412251.081.

NOTE: This TEM image shows the base metal at the left hand side of the image, the darkest layer is a gold-palladium coating deposited during the sample preparation process. The area between the Alloy 22 substrate and the gold-palladium coating is the region of interest. It is composed of an approximately 6 to 7 nm compact oxide close to base metal and a thicker, porous (light) region. The porous oxide is thought to be a silica scale.

Figure N-9. Cross-Sectional TEM Image of Sample DEA496

XPS depth profiling was used to determine the metal and oxygen composition across the oxide. The intensity versus sputter time is shown in Figure N-10a. The intensities were normalized by the elemental sensitivity factors for each energy range. Unfortunately, high-resolution silicon windows were not added to the XPS depth profile, so the silicon composition cannot be seen as a function of depth. However, the low-resolution scan obtained prior to starting the depth profiling showed the presence of silicon at the surface. Because a major constituent is missing, the intensities were not converted to atomic concentrations.

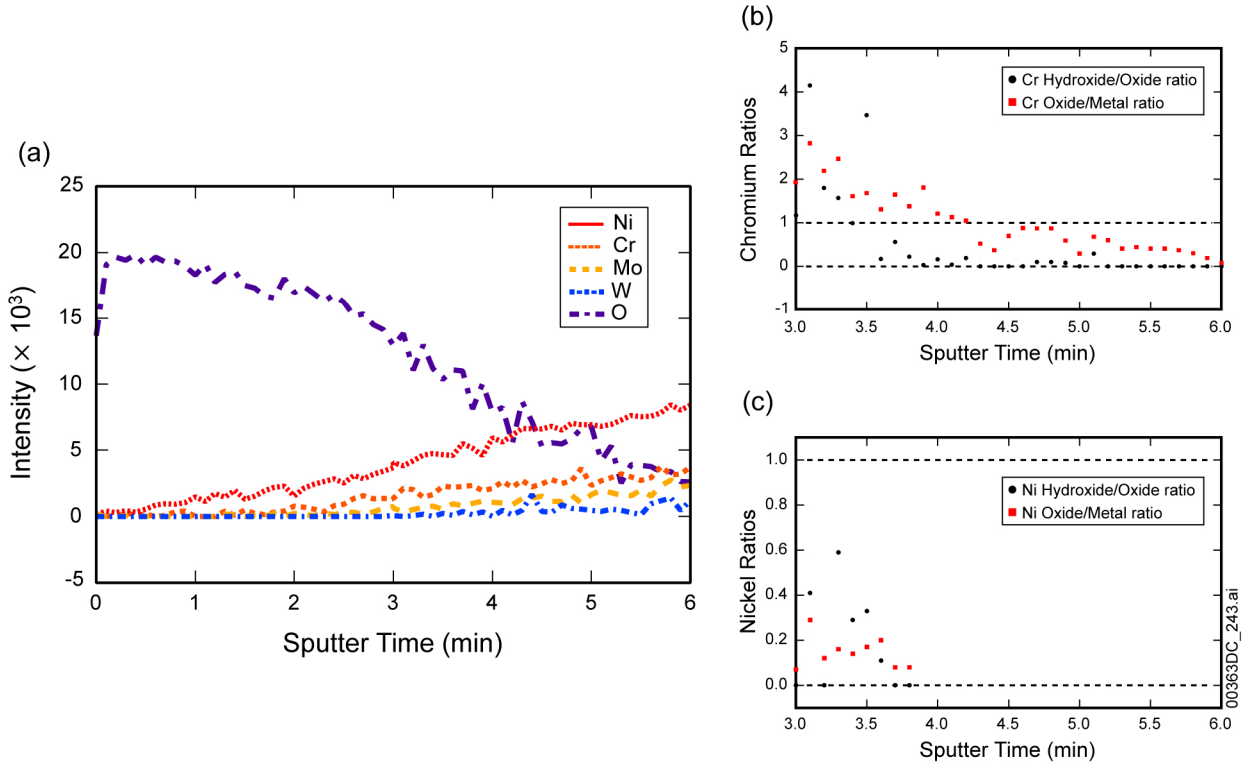

Source: DTN: LL040501112251.094.

Figure N-10. (a) XPS Depth Profile across the Surface Oxide on Sample DEA465; Ratios of the Atomic Concentrations in the Chromium (b) and Nickel (c) Regions

At the deepest sputter point (6 minutes), the spectra have metal peaks but the metal concentrations have not yet leveled off to constant values as expected for the base metal. Also, the oxygen intensities are almost zero. Both of these points suggest that the sputtering has just crossed the oxide but has not penetrated deeply into the metal yet. The first half of the profile is dominated by the porous oxide, which is attributed to silica scale. The second half of the profile contains the compact oxide layer at the metal surface. In this second region, the chromium and nickel regions were fit to determine the relative contributions of the hydroxide, oxide, and metal species. The chromium ratios (Figure N-10b) show that the oxide to metal ratio is greater than one midway through the sputtering and, as expected, trends to zero at the metal interface. In the range where chromium oxide exists (i.e., where the oxide to metal ratio is greater than one), the hydroxide to oxide ratio trends from greater than one to near zero. The nickel peaks were also fit (Figure N-10c), but the hydroxide and oxide components were too small to be fit over the entire range. As found in the chromium speciation, more nickel hydroxide was found in the regions

farther from the metal. Taken together, these ratios suggest that the oxide at the metal surface is predominantly chromium oxide with some nickel. The oxide surface away from the metal has a hydroxide component.

Summary of Oxides Formed as a Function of pH and Applied Potential–In all environments tested, a stable, conformal oxide was formed that passivated the surface, preventing active dissolution of the metal. The oxides were dense and compact with strong adhesion to the surface and, due to this fact and the small thicknesses involved (2 to 5 nm), were mechanically stable and did not spall. The exception to this is a thick porous nickel oxide which formed at higher potentials over a dense chromium oxide underlayer in solutions near pH 8 (±0.5). However, the passivity of the metal is due to the chromium oxide underlayer, so if the porous layer spalled off it would have no effect on the passivity of the metal. In all of the environments studied, a dense, conformal, predominantly chromium oxide adheres to the metal surface. This oxide provides stability for the metal in the tested environments.

Near pH 3 (±0.4), the oxide is a thin (about 4 nm thick) conformal layer. At higher potentials within the passive plateau, the oxide becomes thinner but more compact and uniform. The oxide is predominantly chromium with some molybdenum, nickel, and tungsten.

At pH near 8 (±0.5), the oxide in the passive region is similar to that found in the acidic region; it is mostly chromium oxide with lower concentrations of molybdenum and nickel. At higher voltages, the oxide transforms into a film with two distinct layers, with a compact oxide (about 4 nm thick) near the surface and a porous structure (between 30 and 40 nm thick) at the oxide–solution interface. The outer porous oxide is almost entirely nickel oxide with some iron oxide. Similar oxide films were formed in SCW (DTNs: LL030300912251.036 and LL030301412251.038).

At basic pH, the surface has a coating of porous silica scale due to dissolution from the glassware. However, silica is present in a range of relevant brines and is observed to precipitate out of solution at the oxide–solution interface. The oxide underlying the silica is compact and is composed primarily of chromium oxide. In all cases, it appears that a noncrystalline chromium oxide with oxidation state 3+ is responsible for the passive behavior of the metal.

N.4.6 Oxide Growth Rate

The kinetics of passive film growth on metals are often investigated by following the decay of the anodic current (i) with time (t) upon potentiostatic polarization in the passive region (MacDougall 1983; Bulman and Tseung 1972). In general, the thickness of a film is proportional to the anodic charge (Q). The rate of film growth at a constant potential decreases exponentially with increasing thickness, such that an expression of the form

$$i = Ae^{\left(-\frac{Q}{B}\right)} \qquad \text{(Eq. N-1)}$$

where A and B are constants that depend on parameters of the film, describes the relationship between current and film thickness. By taking the logarithm of both sides of Equation N−1, it is found that $\log(i) \propto Q$. Therefore, if the film growth is indeed logarithmic, a plot of $\log(i)$ versus $\log(t)$ should be linear.

Despite considerable work that has been carried out and the available literature describing the formation of anodic oxide films on metals, no universally accepted model has been devised to explain the mechanism of anodic oxide growth. However, two theories: the high field model and the point defect model, have been advanced to account for the properties of experimentally observed anodic passive films.

Quantitative descriptions of the kinetics of film formation date back to the work of Cabrera and Mott (1949). The most basic approach assumes that ion transport through the film is controlled by the electric field across the film. The higher that the field is, the lower the activation energy for ion or vacancy hopping is (this is called the high-field mechanism) (Bulman and Tseung 1972). Consequently, the rate determining reactions can be attributed to the potential difference between the metal–oxide interface (Cabrera and Mott 1949) and the oxide–environment interface (Fehlner and Mott 1970). When the electric field at the surface can no longer reduce the activation barrier for diffusion, the oxide reaches a limiting thickness value.

The point defect model has also been proposed to explain the kinetics of passive film growth (Macdonald 1999). According to the model, the anodic current that passes after the first few seconds of passivation is mainly associated with breakdown at local weak points in the oxide film and subsequent anodic repassivation. Repassivation involves both reformation of the oxide and metal dissolution. Since the current is a measure of the resistance of the oxide toward local breakdown, its logarithmic decrease with time suggests a logarithmic increase in the state of perfection of the oxide film (MacDougall 1983).

In Figure N-11, log(i) versus log(t) plots are shown for anodic oxide growth on Alloy 22 in pH 7.5, 1-mol/L NaCl solution at 90°C for various potentials. For each measurement, the potential was changed instantaneously from the open circuit potential to the indicated potential and the decay of i was subsequently monitored for approximately 16 hours. The extent of linearity of the log(i) versus log(t) plot is indicated by extrapolating the initial readings to longer polarization times (as indicated by the dashed line in Figures N-11 and N-12). At a potential of 150 mV versus Ag/AgCl, the log(i) versus log(t) relationship is approximately linear for the duration of the experiment time. At potentials of 400 and 700 mV, the current after a long time (10^4 seconds) eventually deviates from the linear behavior (DTN: LL040501012251.093).

In Figure N-12, log(i) versus log(t) plots are shown for Alloy 22 in pH of 2.8, 1-mol/L NaCl solution at 90°C at potentials of 200 mV and 500 mV. At both potentials, the curve deviates from linearity markedly earlier (10^3 seconds) than in the pH 7.5 solution. The results indicate that the cutoff time for the linear decrease of log(i) with log(t) increases with decreasing solution aggressiveness and increasing potential. MacDougall (1983) reports similar results for the passivation of nickel.

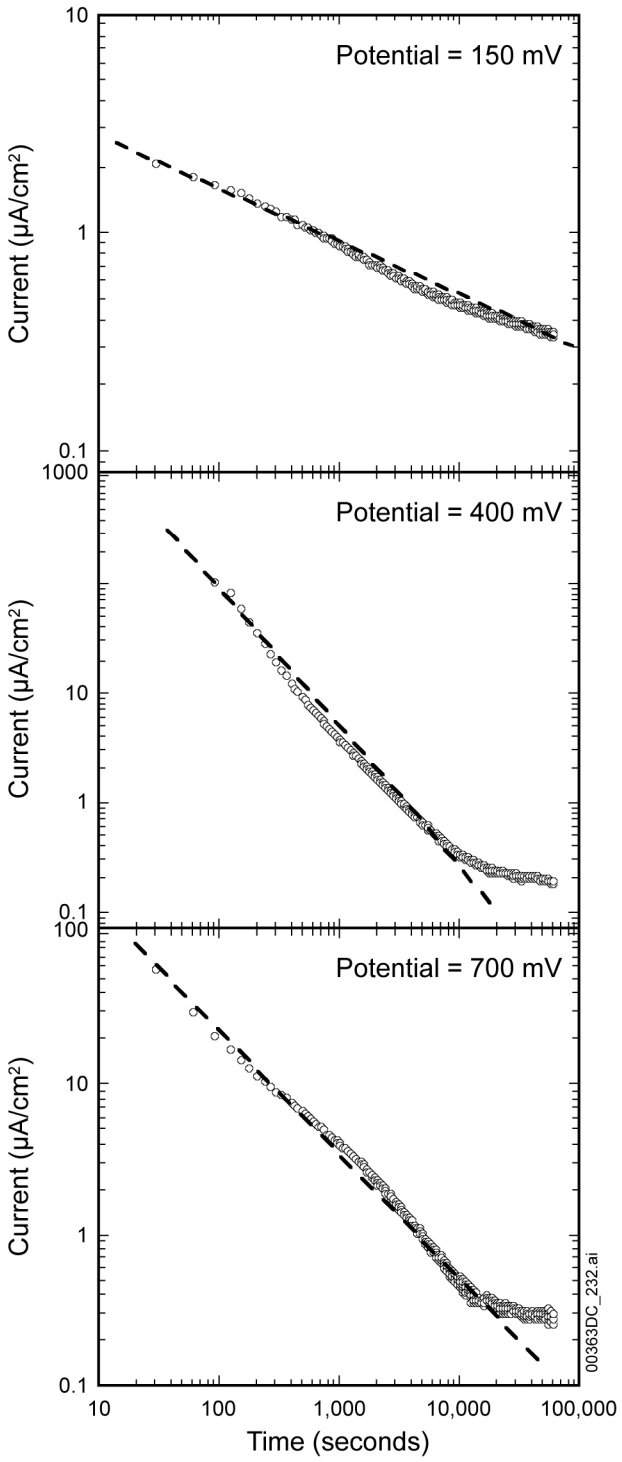

Source: DTN: LL040501012251.093.

Figure N-11. log(*i*) versus log(*t*) Plots for Alloy 22 in 1 mol/L NaCl with pH 7.5, at 90°C, at Potentials of 150 mV (top), 400 mV (middle), and 700 mV (bottom) versus Ag/AgCl

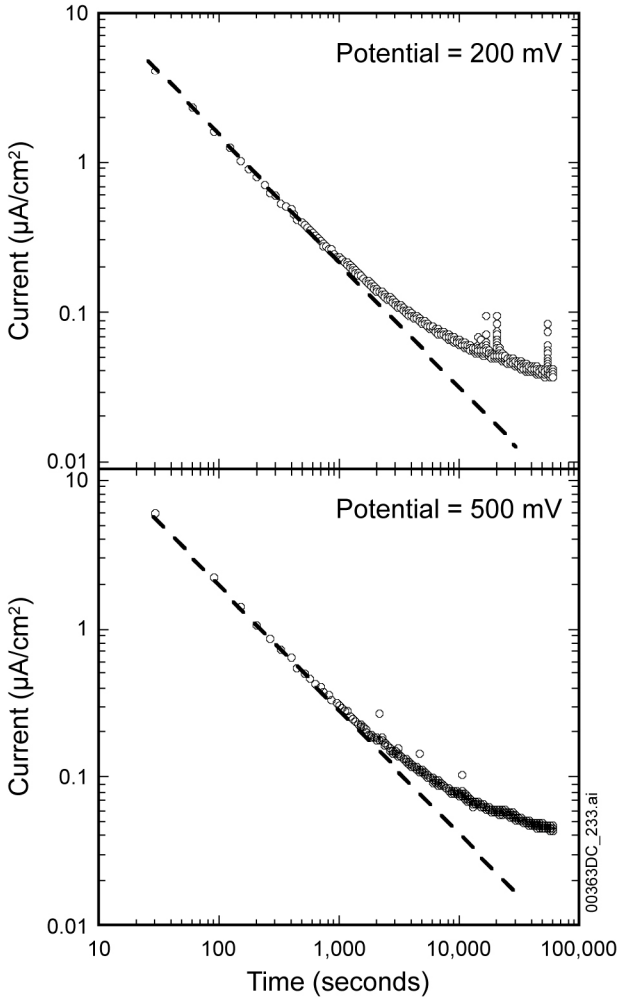

Source: DTN: LL040501012251.093.

Figure N-12. log(*i*) versus log(*t*) Plots for Alloy 22 in 1 mol/L NaCl with pH 2.8, at 90°C, at Potentials of 200 mV (top) and 500 mV (bottom) versus Ag/AgCl

The results for the passive film growth on Alloy 22 presented in Figure N-11 and Figure N-12 indicate that for a large portion of time, the relationship between log(*i*) and log(*t*) is linear. Consequently, the film growth is logarithmic. This claim is further substantiated by tests done at the LTCTF, which show films after 5 years in aqueous environments with similar thickness as those from the short studies presented. These films have strong adhesion to the surface, are mechanically stable, and show no evidence of spalling. To model the observed results, the point defect model is utilized.

Deviations from linearity in log(*i*) versus log(*t*) have been discussed by MacDougall (1983) using the point defect model. The essence of the model is that oxide perfection (increase in stability) occurs at local defect sites, where dissolution and subsequent repassivation results in a more perfect oxide. The lifetime of the oxides at these sites depends on the aggressiveness of the solution and the applied potential. The logarithmic increase in film stability with time can be explained by the fact that the local oxide lifetime increases rapidly as the oxide becomes more perfect. In the early stages of passivation, the oxide is able to perfect itself easily because the

lifetimes required for an increase in local stability are short. Once the film reaches a higher level of perfection, longer dwell times are required for a further increase in perfection. Oxide dwell times are longer in less aggressive solutions (e.g., pH 7.5, 1 mol/L NaCl), thus, the oxide can achieve a very high state of perfection. Deviation from linearity in the log(i) versus log(t) plot is only observed after long times of polarization (as in Figure N-11). Conversely, in more aggressive solutions, localized chemical dissolution of the oxide is rapid, and the local dwell times are short, leading to a rapid increase in oxide perfection and, therefore, early deviation from linearity in log(i) versus log(t). Eventually, a steady state may be reached where no further increase in perfection can occur and the anodic current is thus constant in time (as in Figure N-12).

In conclusion, the linearity of log(i) versus log(t) plots, in conjunction with data from the LTCTF, provides conclusive evidence that the passive oxide on Alloy 22 grows logarithmically with time. By utilizing the point defect model, physical insight into the kinetics of growth was gained. Deviations in the linearity of log(i) versus log(t) plots at longer times, in more aggressive solutions and higher potentials, were due to rapid chemical dissolution of the oxide enabling a steady state to be reached where the anodic current becomes constant in time.

N.4.7 Oxide Stability as a Function of pH and Applied Potential

To address the question of film stability, two electrochemical metrics are used: the polarization resistance and the current density after holding at fixed voltage for a time period. These are converted to a corrosion rate (or penetration rate) so that they can be compared. However, they do not all measure equivalent processes. The polarization resistance measurement provides an instantaneous corrosion rate, whereas the current density after 16 to 20 hours gives a value closer to the steady state corrosion rate. Neither of these will be the same as values obtained from weight-loss measurements, which integrates the corrosion rate over the history of the specimen. Nevertheless, within each metric, different environments can be compared. Because electrochemical results did not differ in the buffered and multi-ionic solutions, they are grouped in these data sets.

Polarization Resistance as a Metric–At open circuit potential, the polarization resistance can be measured. This in turn can be converted to a corrosion rate following guidelines set forth in ASTM G 59-97, *Standard Test Method for Conducting Potentiodynamic Polarization Resistance Measurements*. Most samples were held at open circuit potential for 24 hours prior to measuring the polarization resistance and thus reflect a surface that has partially equilibrated with the solution. The polarization resistance measures an instantaneous corrosion rate at this point in time. The open circuit potential and presumable polarization resistance continue to evolve over time, but the majority of the change occurs over the first 24 hours. The data are plotted against the pH of the solution in Figure N-13a, and against the open circuit potential in Figure N-13b. The average values and standard deviations for the base metal samples are 2.1 ±1.2 μm/yr, 0.3 ±0.3 μm/yr, and 1.5 ±0.4 μm/yr for pH 3, 8, and 11, respectively (DTN: LL040500812251.091). The average values and standard deviations for the weld metal samples are 1.0 ±0.5 μm/yr, 0.11 ±0.03 μm/yr, and 0.17 ±0.03 μm/yr for pH 3, 8, and 11, respectively (DTN: LL040607512251.109). The major findings are: (1) the average polarization resistance corrosion rate is higher in solutions near pH 3 and 11 than pH 8, (2) the welds do not differ significantly from the base metal, and (3) the corrosion rate does not trend with open circuit potential.

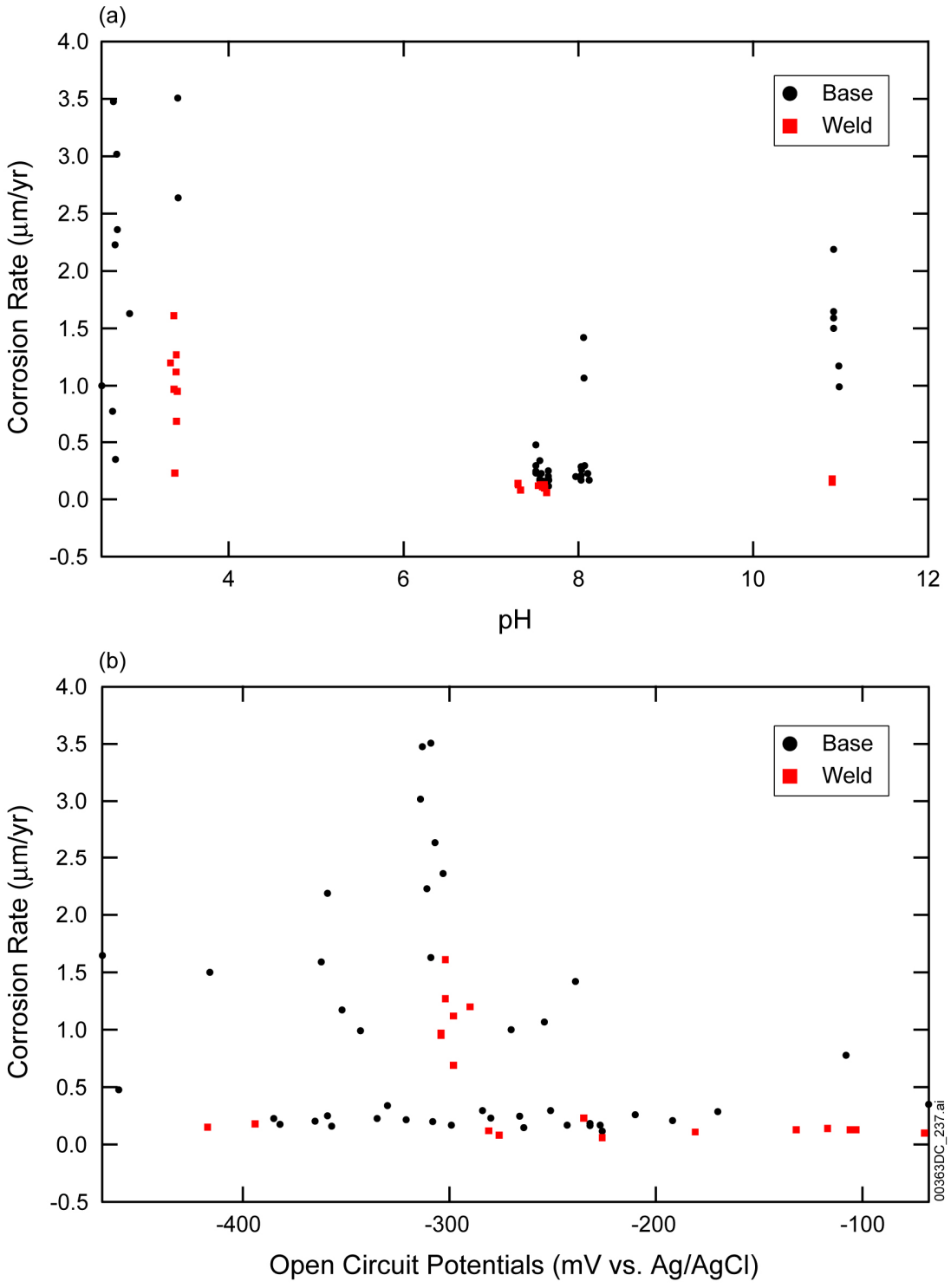

Source: DTN: LL040500812251.091, LL040607512251.109.

NOTE: The polarization resistance corrosion rate is plotted against pH (a) and (b) shows the open circuit potentials at which the tests were performed. Voltages are versus Ag/AgCl electrode.

Figure N-13. Corrosion Rate as Determined by the Polarization Resistance Shown as a Function of the Solution pH

Corrosion Rate from the Current–When Alloy 22 is held at fixed potential within the passive region, its current decreases over time. Figure N-11 illustrates the current response as the metal equilibrates with a pH 7.5 solution. The current response has two regions: the first associated with oxide growth and the second associated with the steady state. The steady state current gives the balance between dissolution of the oxide and reformation of the passive film.

In this comparison, the current after 16 to 20 hours is converted to a corrosion rate using ASTM G 102-89, *Standard Practice for Calculation of Corrosion Rates and Related Information from Electrochemical Measurements*. In most cases, this time duration is sufficient for the current response to be beyond the quickly changing oxide growth region. In Figure N-11, it can be seen that the sample held at 150 mV is still in the oxide growth region, whereas samples held at 200 mV (not shown), 400 mV, and 750 mV are not. However, the time duration may not be long enough for these values to reflect a true steady state current value. To determine this, these values would need to be compared with long-term tests.

Figure N-14 shows the corrosion rates plotted as a function of pH and applied voltage. The average values and standard deviations for the base metal are 1.9 ±3.0 μm/yr, 2.0 ±1.7 μm/yr, and 1.9 ±1.6 μm/yr for pH 3, 8, and 11, respectively (DTN: LL040500712251.090). Too few weld metal samples were tested potentiostatically for meaningful statistical calculations. The four samples that were tested at pH 3 had final current corrosion rates below 0.31 μm/yr at both 200 and 400 mV potentials (two samples tested at each potential). At pH 8, the final current corrosion rates were below 0.8 μm/yr at both 200 and 400 mV potentials (two samples tested at each potential). Two samples were tested at 650 mV, which is approaching transpassive dissolution; one of the samples had a corrosion rate of 2.3 μm/yr, and the other had a corrosion rate of 21.2 μm/yr. This variation could be due to an experimental outlier or proximity of the transpassive region (DTN: LL040607412251.108). The primary finding is that the corrosion rate does not show strong trends with either pH or voltages for the ranges tested. The pH values tested ranged from 3-12 and include buffered solutions as well as multi-ionic, SAW, SCW, and BSW. The basic solutions had silica deposition from the glassware. The voltages ranged from the open circuit potential to transpassive dissolution. It is interesting to note that even though samples in pH 8 solution have a phase transition that occurs at about 350 mV, the current response after 16 hours is approximately the same for the region with the thin oxide as well as the porous oxide (Figure N-7). The data set also includes several measurements in the transpassive region; these data (at 750 mV and above) have much higher currents and are not shown on the graphs.

As was seen from the discussion of oxide characterization, chromium oxides with chromium in the 3+ oxidation state are the primary species in the barrier layer for the range of pH and potential values tested. The equilibrium speciation modeling suggests that the Cr_2O_3 that forms at pH 2.8, and the $NiCr_2O_4$ that forms at pH 7.5 may be thermodynamically stable. However, this was only shown for conditions where 1 g of metal was dissolved into 1 kg of NaCl solution. This corresponds to approximately 0.01 mol/L dissolved Alloy 22. In the experiments above, the measured currents provide an estimate of the metal transferred to solution. If the entire current is assumed to be due to metal dissolution, metal concentrations are 10^{-5} to 10^{-6} mol/L. At these concentrations, it is very unlikely that chromium oxides are thermodynamically stable oxide phase.

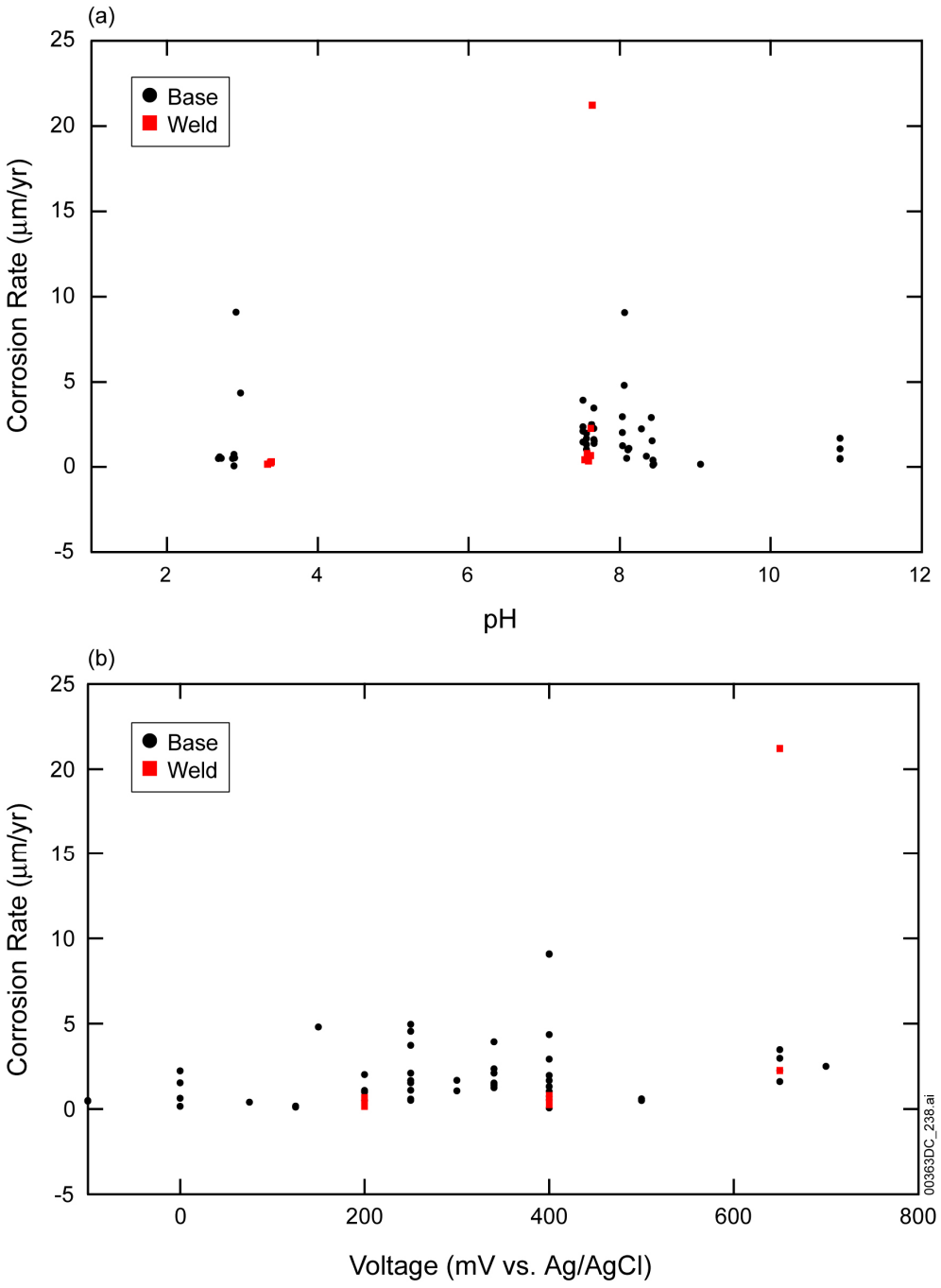

Source: DTN: LL040500712251.090, LL040607412251.108.

NOTE: The final current corrosion rate is plotted against (a) pH and (b) applied voltage. Voltages are versus Ag/AgCl electrode.

Figure N-14. Current after Equilibrating at Constant Potential for 10 to 20 Hours Converted to a Corrosion Rate

In summary, the data show that the currents decay to the microampere range in 18 hours at all solutions tested between the OCP and transpassive dissolution. This implies that an oxide layer forms which inhibits current flow. The data also show that this barrier oxide is predominantly chromium oxide with a chromium(III) oxidation state. It seems unlikely that the oxide is thermodynamically stable given the low concentrations of metal in solution. Taken together, this suggests that a kinetically stable chromium oxide layer forms well before enough metal dissolves into solution to make the solution saturated with respect to the oxide phase. Presumably, if sufficient current were to flow or if the solution volume were small (as might be expected in vapor or water droplets on the waste package surface), then the solution would saturate and the oxide would become thermodynamically stable under fixed conditions.

Several reasons are provided in the literature for the stability of the passive film. Marcus and Maurice (2000) find that the grains of nanocrystalline Cr_2O_3 on Cr (110) have a surface of hydrated chromium hydroxide. They suggest that the hydroxide surface coating acts like cement to limit transport along grain boundaries. Some authors suggest that a bipolar oxide film forms with a net negative charge at the oxide–solution interface and a net positive charge at the metal–oxide interface. The negative net charge reduces the diffusion of negative anions to the oxide/hydroxide surface, and this in turn limits reactions with the metal that rely on anodic current flow. This picture is discussed by Schmuki (2002). The net charge on Alloy 22 has not been measured as part of this work.

If Cr_2O_3 is kinetically rather than thermodynamically stable, then it will dissolve at the surface, and chromium metal will be converted to chromium oxide at the metal–oxide interface. The initial oxidation creates a slight weight gain, but over time the surface dissolution will counteract that gain, and eventually a net weight loss will be observed. At the end of the test, the oxides and scales are removed from the surface of the samples, leaving the bare metal. This is weighed to ascertain the total weight loss due to corrosion. The LTCTF has had specimens in test for over 5 years in solutions with pH 3 to 11. Corrosion rates for both mill annealed and as-welded specimens can be determined from the mass loss. Thus far, the corrosion rates, which are shown in Figure N-15, are between 10^{-3} and 10^{-2} μm/yr. This indicates that the general corrosion rate from the kinetically formed films under the conditions evaluated is sufficiently low to ensure the lifetime of the waste packages.

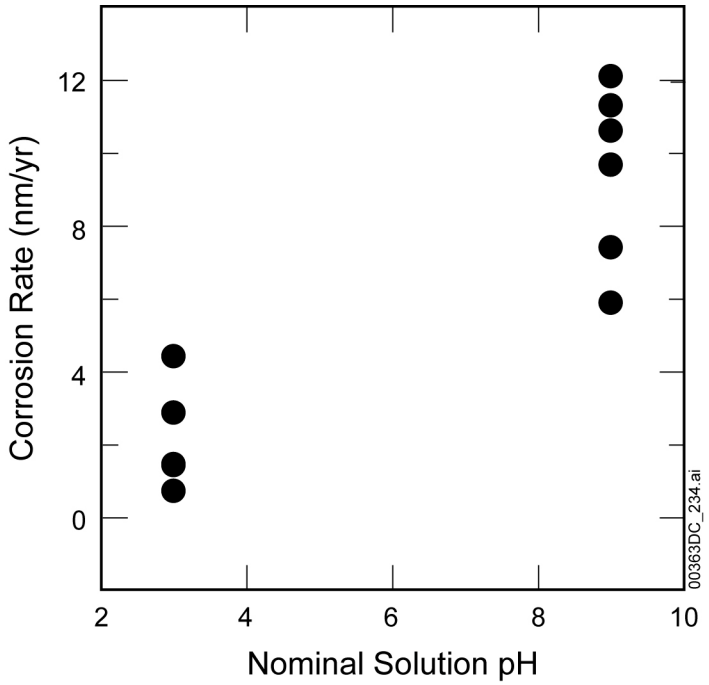

Source: BSC 2003a; DTN: SN0308T0506303.004.

Figure N-15. Corrosion Rate Determined from the Weight Loss of Alloy 22 Mill Annealed and As-Welded Specimens Held in 90°C Simulated Acidified Water (pH of Approximately 3) and Simulated Concentrated Water (pH of Approximately 9 to 11) for More Than 5 Years

N.4.8 Oxide Formation on Solution-Annealed Alloy 22

In the current design plans, the waste package surface will have a surface finish created during the solution annealing step. Therefore, it is important to understand the differences between these surfaces and a polished substrate. To create the solution-annealed substrates, polished samples were placed in an oven held at 1,121°C for 20 minutes. The gas in the ovens was laboratory air. After annealing for 20 minutes, the samples were quickly cooled in a water bath of Millipore (18 Ω·cm) water and dried with compressed air. Optical inspection showed that the surfaces, which are shiny before annealing, turn a matte black after quenching due to a thick oxide scale that forms at the surface. AFM and SEM were used to image the surface morphology; TEM was used to look at the oxide in cross section; EELS was used to determine the composition in cross section.

Electrochemical Response–Potentiodynamic scans for solution-annealed samples in SAW, SCW, and BSW solutions are compared with mirror-polished samples in Figure N-16. In the data shown, the current at a given voltage is lower for the solution-annealed samples in all solutions, except above the anodic peak in SCW. Because only one trial was done for each condition, it is not known how variable these curves are, so a quantitative comparison cannot be provided. In the SCW solution, the anodic peak in the potentiodynamic curve is no longer seen, and the porous oxide film associated with the anodic peak is not found.

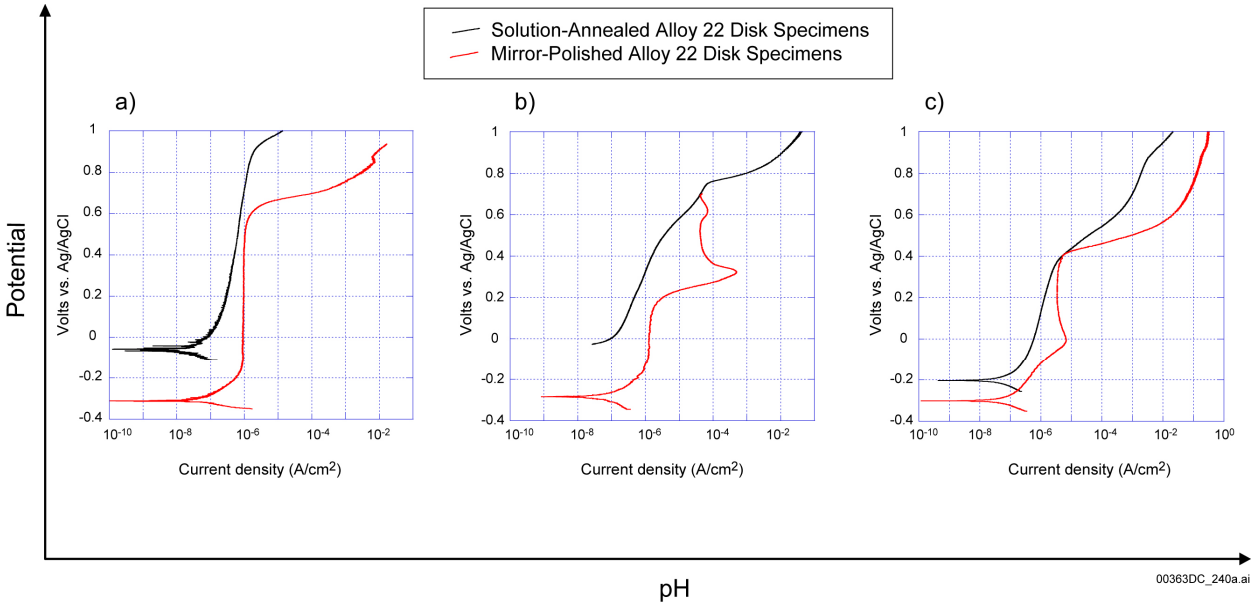

Source: DTNs: LL040505512251.101.

NOTE: Potentiodynamic potential versus current density scans in (a) SAW (annealed: DEA480; polished: DEA492); (b) SCW (annealed: DEA505; polished: DEA1246); and (c) BSW (annealed: DEA481; polished: DEA461).

Figure N-16. Electrochemical Response of Solution-Annealed Versus Mirror-Polished Alloy 22 Disk Specimens

Morphology–Figure N-17a is an AFM image of a freshly polished surface. The underlying grain structure can be seen in this 100 µm by 100 µm scan although the height difference between neighboring grains is less than a nanometer. Figure N-17b shows the same location after the solution-annealing process. The surface is covered with a polycrystalline oxide scale. Interestingly, much of the original metal grain structure can still be observed even after the thick (greater than 1 µm) oxide scale has grown. The same sample is also shown, Figure N-17c, after it has been potentiostatically held in the passive region, at 250 mV in 90°C BSW for about 10 hours. No appreciable morphological changes can be observed due to the electrochemical modification.

After the solution anneal process, many of the grains have grain boundaries that are higher than the plane of the grain. These taller morphologies appear as a lighter color in the AFM images. This suggests that the polycrystalline oxide grows thicker in these regions, presumably due to greater oxygen and metal ion transport in these regions. However, this is not observed on all grain boundaries. The long boundaries typical of adjacent twinned grains shown in the lower right corner of the polished substrate (Figure N-17a) do not stand out after solution annealing.

The surface morphology was also examined using a scanning electron microscope (Figure N-18). At the higher magnification, Figure N-18a, it can be seen that there are two distributions of crystals with different sizes. A relatively uniform, submicrometer-sized set of crystals—as compared with the lower magnification image, Figure N-18b—is concentrated at the grain boundaries, and a broader distribution of crystals with crystal sizes up to several micrometers is concentrated in the center of the grains.

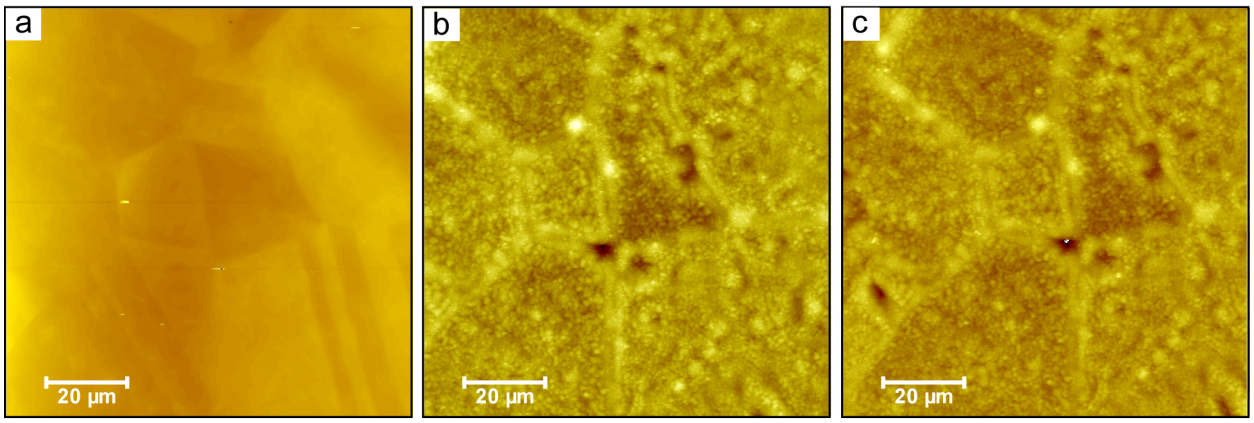

Source: DTN: LL040207612251.077.

Figure N-17. AFM Images of the Surface of Sample DEA497 (a) after Polishing, (b) after the Solution Annealing Process, and (c) after Potentiostatically Holding the Sample at 250 mV in 90°C BSW Solution for about 10 Hours

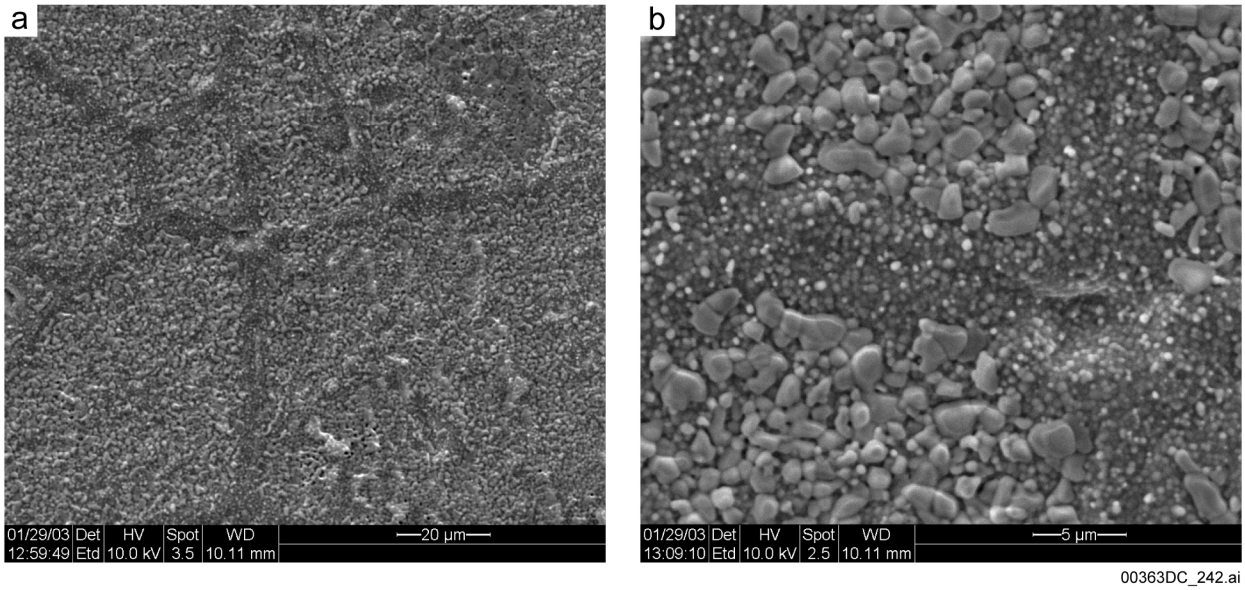

Source: DTN: LL040207412251.075.

Figure N-18. SEM Images of DEA497, a Solution-Annealed Alloy 22 Substrate Shown at Two Scales

Composition of Solution-Annealed Specimens–The composition of the oxide scale was determined using cross-sectional TEM with EELS elemental mapping. Figure N-19a shows a transmission electron micrograph of the cross section between the base metal, through the oxide scale and to the gold (not labeled) and platinum layers that indicate the outer edge of the oxide scale. Figure N-19b shows a composite EELS image of this same region, distinguishing the nickel, iron, and chromium. By comparing with the oxygen map shown below, it is clear that the scale is an oxide where the chromium, iron, and nickel oxides have segregated. Chromium oxide (green) is closest to the base metal and has the greatest thickness (about 0.8 µm). An iron oxide forms a 0.1- to 0.5-µm layer on top of the chromium oxide, and a nickel oxide with similar thickness forms the outer layer.

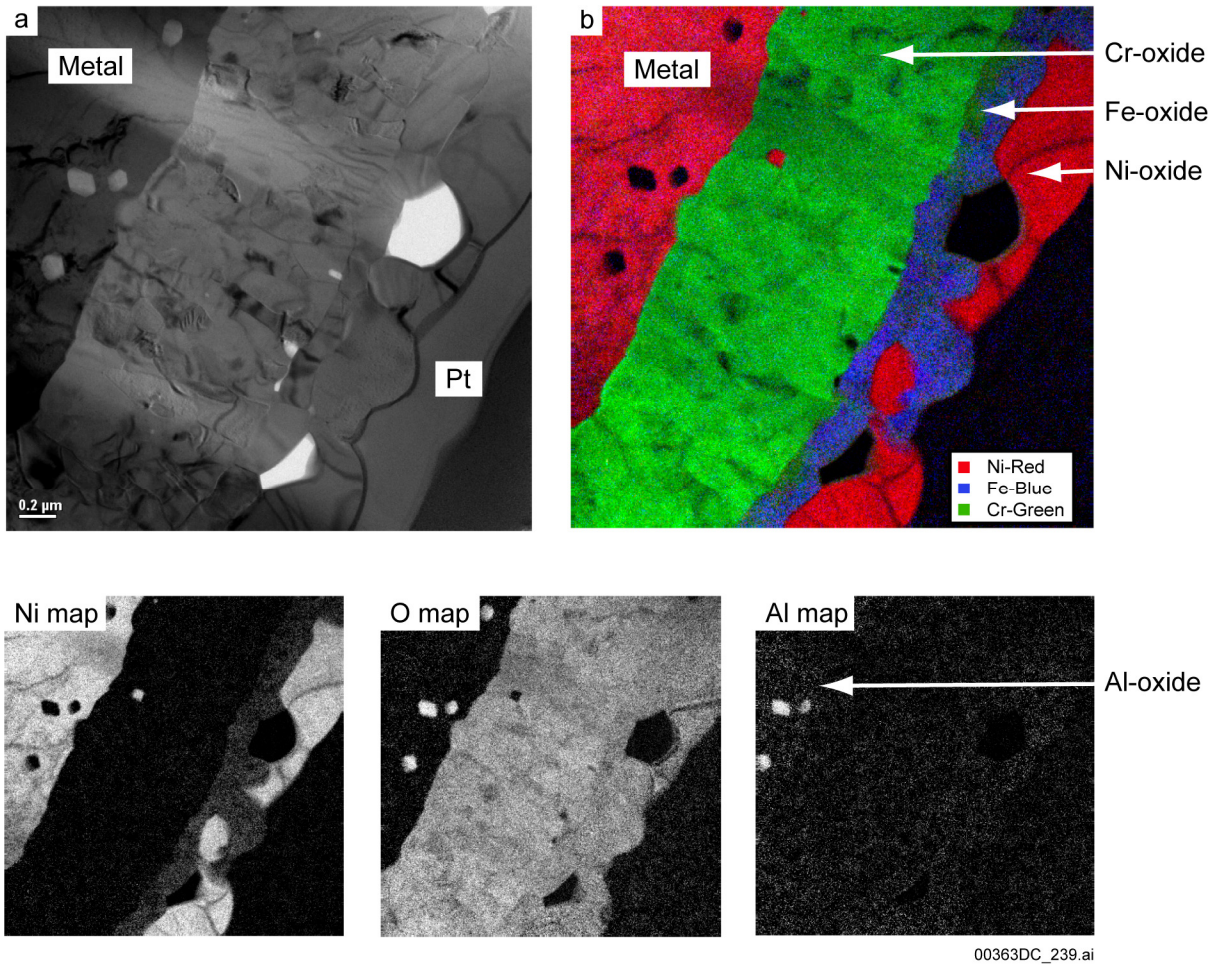

Source: DTN: LL040500512251.088.

NOTE: The TEM image (a) shows the base metal at the upper left corner and the layered structure of the chromium, iron, and nickel oxides that form during the solution anneal process. The oxide shown is greater than 1 µm thick (a 0.2-µm scale bar is shown on the image). Layers of gold (not labeled) and adjacent platinum (lower right corner) are due to the sample preparation process. The composite EELS image (b) of the same area shows nickel, iron, and chromium composition. The oxygen map (d) clearly identifies the scale as oxides. The inclusions that form in the base metal are an aluminum oxide.

Figure N-19. Cross-Sectional View of DEA498, a Solution-Annealed Alloy 22 Substrate with (a) TEM Image, (b) a Composite Electron Energy-Loss Spectroscopy Image of the Same Area, and Individual Maps of Nickel, Oxygen, and Aluminum

The metal–oxide interface, which was flat due to polishing prior to the solution-annealing step, now appears faceted, suggesting that the metal is not consumed uniformly when it is converting to oxide. Additionally, aluminum (presumably as a minor constituent of Alloy 22) diffuses and coalesces into aluminum oxide inclusions in the metal near the metal–oxide interface. A small metallic nickel island can also be seen within the chromium oxide layer.

The oxide scale that forms on Alloy 22 during a solution annealing step was characterized using several methods. The approximately 1-µm thick oxide is composed of layers of chromium oxide, iron oxide, and nickel oxide. The grain boundaries have a smaller polycrystalline grain

structure as compared to the center of the grains. While only a limited number of electrochemical tests were performed, the electrochemical behavior from potentiodynamic scans shows that the scale does not adversely affect the corrosion performance of solution-annealed samples. However, no long-term potentiostatic tests were performed. Oxides that form at lower temperatures (400°C to 750°C) but longer times (years) also have a thick, predominantly chromium oxide scale like the solution-annealed substrates. Based on this observation, studies on annealed samples aged at repository temperatures were not considered necessary. Microstructural evaluation of samples aged at various temperatures in the range of 427°C to 700°C showed that no significant aging will occur at repository relevant temperature (less than 200°C). Low-temperature aging has been shown to produce little or no evidence of precipitation or second phase particles in the grain boundaries or in the matrix and long range ordering (BSC 2003b, Section 8).

N.5 REFERENCES

N.5.1 Documents Cited

Angeliu, T.M. 2001. "Microstructural Characterization of L-Grade Stainless Steels Relative to the IGSCC Behavior in BWR Environments." *Corrosion/2001 56th Annual Conference & Exposition, March 11-16, 2001, Houston, Texas, USA*. Paper No. 01121. Houston, Texas: NACE International. TIC: 254941.

BSC (Bechtel SAIC Company) 2003a. *General Corrosion and Localized Corrosion of Waste Package Outer Barrier*. ANL-EBS-MD-000003 REV 01, with errata. Las Vegas, Nevada: Bechtel SAIC Company. ACC: DOC.20030916.0010; DOC.20031222.0002; DOC.20031222.0001.

BSC 2003b. *Aging and Phase Stability of Waste Package Outer Barrier*. ANL-EBS-MD-000002 REV 01 ICN 0. Las Vegas, Nevada: Bechtel SAIC Company. ACC: DOC.20030807.0004.

Bulman, G.M. and Tseung, A.C.C. 1972. "The Kinetics of the Anodic Formation of the Passive Film on Stainless Steel." *Corrosion Science*, *12*, 415–432. New York, New York: Pergamon Press. TIC: 255893.

Cabrera, N. and Mott, N.F. 1949. "Theory of the Oxidation of Metals." *Reports on Progress in Physics*, *12*, 163–184. London, England: The Physical Society. TIC: 255982.

Cragnolino, G.A.; Pan, Y.-M.; Turner, D.; Pearcy, E. 2004. *Natural Analogs of High-Level Waste Container Materials - Experimental Evaluation of Josephinite*. CNWRA 2004-02. San Antonio, Texas: Center for Nuclear Waste Regulatory Analyses. TIC: 256074.

Fehlner, F.P. and Mott, N.F. 1970. "Low-Temperature Oxidation." *Oxidation of Metals*, *2*, (1), 59–99. New York, New York: Plenum Press. TIC: 256036.

Friend, W.Z. 1980. "Nickel-Chromium-Molybdenum Alloys." Chapter 8 of *Corrosion of Nickel and Nickel-Base Alloys*. New York, New York: Wiley-Interscience. TIC: 256002.

Hodge, F.G. and Wilde, B.E. 1970. "Effect of Chloride Ion on the Anodic Dissolution Kinetics of Chromium–Nickel Binary Alloys in Dilute Sulfuric Acid." *Corrosion*, *26*, (6), 146. Houston, Texas: National Association of Corrosion Engineers. TIC: 255960.

Jabs, T.; Borthen, P.; and Strehblow, H.H. 1997. "X-Ray Photoelectron Spectroscopic Examinations of Electrochemically Formed Passive Layers on Ni-Cr Alloys." *Journal of the Electrochemical Society*, *144*, (4), 1231–1243. Pennington, New Jersey: Electrochemical Society. TIC: 255979.

Lim, A.S. and Atrens, A. 1992. "ESCA Studies of Ni-Cr Alloys." *Applied Physics A: Solids and Surfaces*, *A54*, 343–349. Berlin, Germany: Springer-Verlag. TIC: 255984.

Lin, L.F.; Chao, C.Y.; and Macdonald, D.D. 1981. "A Point Defect Model for Anodic Passive Films. II. Chemical Breakdown and Pit Initiation." *Journal of the Electrochemical Society*, *128*, (6), 1194–1198. Manchester, New Hampshire: The Electrochemical Society. TIC: 246354.

LLNL (Lawrence Livermore National Laboratory) 2003a. *Acceptance Report for Scientific Investigations, for Charles Evans & Associates, Auger Electron Spectroscopy (AES) Surface Analysis Report and X-Ray Photoelectron Spectroscopy for Chemical Analysis Report. EAG Number:* C03H3684. PO BA004609, REL 37250. ACC: MOL.20040322.0165.

LLNL 2003b. *Acceptance Report for Scientific Investigations, for Charles Evans & Associates, X-Ray Photoelectron Spectroscopy (XPS)/Electron Spectroscopy For Chemical Analysis (ESCA) Surface Analysis Report and Auger Electron Spectroscopy (AES) Surface Analysis Report.* EAG Number: C03H2677. PO BA004609, REL 34672 Rev 01. ACC: MOL.20040210.0470.

Lloyd, A.C.; Shoesmith, D.W.; McIntyre, N.S.; and Noel, J.J. 2003. "Effects of Temperature and Potential on the Passive Corrosion Properties of Alloys C22 and C276." *Journal of the Electrochemical Society*, *150*, (4), B120–B130. New York, New York: Electrochemical Society. TIC: 255963.

Macdonald, D.D. 1999. "Passivity—The Key to Our Metals-Based Civilization." *Pure and Applied Chemistry*, *71*, (6), 951–978. Oxford, England: Blackwell Science. TIC: 249795.

MacDougall, B. 1983. "Interpretation of Log i–Log t Relationships for Nickel Passivation." *Journal of the Electrochemical Society*, *130*, (1), 114–117. Manchester, New Hampshire: The Electrochemical Society. TIC: 255980.

Marcus, P. and Grimal, J.M. 1992. "The Anodic Dissolution and Passivation of Ni-Cr-Fe Alloys Studied by ESCA." *Corrosion Science*, *33*, (5), 805–814. Oxford, England: Pergamon. TIC: 255959.

Marcus, P. and Maurice, V. 2000. "Passivity of Metals and Alloys." Chapter 3 of *Corrosion and Environmental Degradation.* Schütze, M., ed. Volume I. Materials Science and Technology Volume 19. New York, New York: Wiley-VCH. TIC: 249831.

Olsson, C.-O.A. and Landolt, D. 2003. "Passive Films on Stainless Steels–Chemistry, Structure, and Growth." *Electrochimica Acta*, *48*, 1093–1104. Oxford, England: Pergamon. TIC: 255964.

Orme, C. 2003a. Oxide Characterization. Scientific Notebook SN-LLNL-SCI-465-V1. ACC: MOL.20031024.0068.

Orme, C. 2003b. Oxide Characterization. Scientific Notebook SN-LLNL-SCI-465-V2. ACC: MOL.20031209.0148; MOL.20031110.0174.

Orme, C. 2004. Oxide Characterization. Scientific Notebook SN-LLNL-SCI-465-V3. ACC: MOL.20040520.0266.

Piron, D.L.; Koutsoukos, E.P.; and Nobe, K. 1969. "Corrosion Behavior of Nickel and Inconel in Acidic Chloride Solutions." *Corrosion*, *25*, (4), 151. Houston, Texas: National Association of Corrosion Engineers. TIC: 255981.

Pourbaix, M. 1974. *Atlas of Electrochemical Equilibria in Aqueous Solutions.* Houston, Texas: National Association of Corrosion Engineers. TIC: 208955.

Qian, S., Newman, R.C., and Cottis, R.A. 1990. "Validation of a Percolation Model for Passivation of Fe-Cr Alloys: Two-Dimensional Computer Simulations." *Journal of the Electrochemical Society*, *137*, (2), 435–439. Manchester, New Hampshire: The Electrochemical Society. TIC: 246354.

Schlueter, J. 2000. "U.S. Nuclear Regulatory Commission/U.S. Department of Energy Technical Exchange and Management Meeting on Container Life and Source Term (September 12-13, 2000)." Letter from J. Schlueter (NRC) to S. Brocoum (DOE/YMSCO), October 4, 2000, with enclosure. ACC: MOL.20010731.0161.

Schmuki, P.J. 2002. "From Bacon to Barriers : A Review on the Passivity of Metals and Alloys." *Journal of Solid State Electrochemistry*, *6*, 145–164. Berlin, Germany: Springer-Verlag. TIC: 255958.

Schmutz, P. and Landolt, D. 1999. "In-Situ Microgravimetric Studies of Passive Alloys: Potential Sweep and Potential Step Experiments with Fe-25Cr and Fe-17Cr-33Mo in Acid and Alkaline Solution." *Corrosion Science*, *41*, 2143–2163. New York, New York: Pergamon Press. TIC: 255961.

Sieradzki, K. and Newman, R.C. 1986. "A Percolation Model for Passivation in Stainless Steels" *Journal of the Electrochemical Society*, *133*, (9), 1979–1980. Manchester, New Hampshire: The Electrochemical Society. TIC: 255985.

N.5.2 Codes, Standards, and Regulations

ASTM G 59-97. 1998. *Standard Test Method for Conducting Potentiodynamic Polarization Resistance Measurements.* West Conshohocken, Pennsylvania: American Society for Testing and Materials. TIC: 249897.

ASTM G 102-89 (Reapproved 1999) 1989. *Standard Practice for Calculation of Corrosion Rates and Related Information from Electrochemical Measurements.* West Conshohocken, Pennsylvania: American Society for Testing and Materials. TIC: 249897.

N.5.3 Data, Listed by Data Tracking Number

LL030300912251.036. Transmission Electron Microscopy (TEM) Images of Oxide Film on Alloy 22 during Transpassive Dissolution in Simulated Concentrated Water (SCW). Submittal date: 03/20/2003.

LL030301412251.038. Atomic Force Microscope (AFM) Images of Oxide Formation on Alloy 22 (UNS N06022). Submittal date: 05/24/2003.

LL040206412251.071. Atomic Force Microscopy Images of Various Ni-Cr-Mo Alloys Held Potentiostatically in 1 M NaCl Solutions of Various pH Values. Submittal date: 03/18/04.

LL040206512251.072. Auger Electron Spectroscopy Data from Various Ni-Cr-Mo Alloys Held Potentiostatically in 1 M NaCl Solutions of Various pH Values. Submittal date: 04/16/04.

LL040206612251.073. Electrochemical Behavior of Various Ni-Cr-Mo Based Alloys in 1 M NaCl Solutions of Various pH Values. Submittal date: 03/10/04.

LL040206712251.074. X-Ray Photoelectron Spectroscopy Data from Various Ni-Cr-Mo Alloys Held Potentiostatically in 1 M NaCl Solutions of Various pH Values. Submittal date: 04/16/04.

LL040207412251.075. Scanning Electron Microscopy Images for Various Alloy 22 Samples after Corrosion Testing. Submittal date: 03/10/04.

LL040207512251.076. Electrochemical Behavior of Alloy 22 in SAW, BSW, SCW, and 1 M NaCl Solution Buffered to pH 8. Submittal date: 03/29/04.

LL040207612251.077. Atomic Force Microscopy (AFM) Images of Various Ni-Cr-Mo Alloys Held Potentiostatically in Various Solutions. Submittal date: 03/29/04.

LL040308412251.081. Transmission Electron Microscopy (TEM) Data from Various Alloy 22 Samples after Corrosion Testing. Submittal date: 03/29/04.

LL040500512251.088. Transmission Electron Microscopy Data from Various Alloy 22 Samples after Corrosion Testing. Submittal date: 05/18/2004.

LL040500712251.090. Final Current Corrosion Rates of Alloy 22 in 1 M Sodium Chloride Held at Various pH Values. Submittal date: 05/10/2004.

LL040500812251.091. Polarization Resistance Corrosion Rates of Alloy 22 in 1 M Sodium Chloride Held at Various pH Values. Submittal date: 03/10/2004.

LL040500912251.092. Determining Oxide Thicknesses by Analysis of Cross-Sectional Transmission Electron Microscopy (TEM) Images. Submittal date: 05/24/2004.

LL040501012251.093. Alloy 22 Oxide Growth Kinetics as a Function of pH and Potentiostatic Voltage by Analysis of Log Current Density vs. Log Time Plots. Submittal date: 05/02/04.

LL040501112251.094. Depth Analysis of DEA465 Using X-Ray Photoelectron Spectroscopy. Submittal date: 05/31/2004.

LL040501212251.095. Depth Analysis of DEA495 Using X-Ray Photoelectron Spectroscopy. Submittal date: 06/08/2004.

LL040502712342.006. Equilibrium Calculations of Oxide Products from Reaction of 1 g Alloy 22 with ~1 kg of 1M NaCl at 90°C for KTI 1.08/1.09. Submittal date: 05/24/2004.

LL040505512251.101. Electrochemical Behavior of Alloy 22 in Brine Solutions of Various pH Values. KTI 1.08/1.09. Submittal date: 06/29/2004.

LL040607412251.108. Final Current Corrosion Rates of Alloy 22 Weld Specimens in Solutions with Various pH Values. KTI 1.08/1.09. Submittal date: 06/30/2004.

LL040607512251.109. Polarization Resistance Corrosion Rates of Alloy 22 Weld Specimens in Solutions with Various pH Values. KTI 1.08, 1.09. Submittal date: 07/01/2004.

SN0308T0506303.004. Updated General Corrosion Model and Analyses of Waste Package Outer Barrier. Submittal date: 08/20/2003.